This is the peer-reviewed, final accepted version for American Mineralogist, published by the Mineralogical Society of America.
The published version is subject to change. Cite as Authors (Year) Title. American Mineralogist, in press.
DOI: https://doi.org/10.2138/am-2022-8884. http://www.minsocam.org/

Revision 1

The 450 nm (2.8 eV) cathodoluminescence emission in quartz and its relation to structural defects and Ti contents

Jens Götze[1,*], Colin MacRae[2], Yuanming Pan[3], Nicholas C. Wilson[2], Aaron Torpy[2], Andreas Audédat[4]

[1]Institute of Mineralogy, TU Bergakademie Freiberg, Brennhausgasse 14, 09599 Freiberg, Germany

[2]CSIRO Mineral Resources, Bayview Avenue, Clayton, VIC, 3168, Australia

[3]Department of Geological Sciences, University of Saskatchewan, Saskatoon, Saskatchewan S7N 5E2, Canada

[4]Bavarian Geoinstitute, University of Bayreuth, Universitätsstrasse 30, 95447 Bayreuth, Germany

ABSTRACT

The origin of the common blue 450 nm (2.8 eV) cathodoluminescence (CL) emission in natural and synthetic quartz has been investigated by a combination of CL microscopy and spectroscopy, electron paramagnetic resonance (EPR) spectroscopy, and trace-element analysis by microprobe analysis as well as inductively coupled plasma-mass spectrometry (ICP-MS). The study shows that the appearance of the ~450 nm emission band can be attributed to two different defects in quartz. Firstly, a transient luminescence can be explained by structural defects in oxygen deficient quartz. The luminescence model implies self-trapped exciton (STE) emission related to oxygen vacancies. This type of CL emission is frequent in high-purity synthetic quartz and natural quartz of hydrothermal origin. Secondly, in Ti-rich quartz from natural samples (e.g. quartz phenocrysts in rhyolites) and synthetic quartz of Ti-diffusion experiments, an additional 450 nm (2.8 eV) emission was detected which is stable under the electron beam. The intensity of this ~450 nm emission band correlates with the

concentration of trace Ti in quartz, and substitutional Ti^{4+} at the Si^{4+} position was proved by EPR spectroscopy. In quartz crystals with elevated Ti concentrations both intrinsic and extrinsic blue CL emissions at ~450 nm can coexist hindering a thorough characterization and quantification of the CL signal. A reliable distinction of the two different CL emission bands is possible by fitting the peaks of the CL spectra, and the peak width of the 450 nm emission can be used to differentiate the STE from the Ti^{4+} emission. However, the definitive technique is through the observation of CL peak shape change over time at a point by collecting a time series of CL spectra in conjunction with EPR spectroscopy and trace-element analysis of the Ti concentration.

Keywords: Cathodoluminescence (CL), Hyperspectral CL, quartz, blue CL emission, electron paramagnetic resonance (EPR), Ti concentration

INTRODUCTION

Quartz (low-temperature α-quartz) is the most important SiO_2 polymorph in nature, which occurs as a frequent constituent in almost all rock types and also represents an economically important silica raw material. Therefore, the knowledge of specific properties of quartz is indispensable for many mineralogical and geological investigations. Cathodoluminescence (CL) studies of quartz constitute a powerful method, which enables the visualization of the defect structure and reveals internal features, which are not discernible by other analytical methods (Ramseyer et al. 1988; Götze et al. 2001; Götze 2012).

The CL emission of quartz is variable and in general caused by various point defects including both pure lattice defects (e.g. related to oxygen and silicon vacancies) and substitutional trace elements. The relation of specific luminescence emission bands to different defect centres causes a diversity of CL characteristics and visible CL colours in dependence on the processes of mineral formation or alteration (Ramseyer et al. 1988; Götze

et al. 2001, 2021). Therefore, the knowledge about the origin of different luminescence centers can help to reconstruct geological processes and to reveal different growth generations or secondary alteration, which cannot be discerned by optical or electron microscopy (e.g., Zinkernagel 1978; Ramseyer et al. 1988; Ramseyer and Mullis 1990; Watt et al. 1997; Götze et al. 2001, 2005, 2013, 2015, 2017, 2021; Van den Kerkhof et al. 2004; Müller et al. 2005, 2009; Landtwing and Pettke 2005; Rusk et al. 2006, 2008; Krickl et al. 2008; Götze 2009; Jourdan et al. 2009; Lehmann et al. 2009; Götte et al. 2011; Cerin et al. 2017; Götze and Hanchar 2018).

The most common CL emission bands in natural quartz are bands with maxima at ca. 450 and 650 nm (Ramseyer et al. 1988; Götze et al. 2001; Götze 2009). The visible luminescence colors of quartz in most igneous and metamorphic rocks as well as in some authigenic quartz depend on the relative intensities of these two dominant emission bands. Because of the ubiquitous occurrence of the blue 440–450 nm (2.75–2.8 eV) CL emission in synthetic and natural quartz of all rock types, there is an ongoing discussion concerning the defects responsible for this luminescence. Several studies provide strong indication that the ~450 nm emission band is related to oxygen deficiency centres (ODC) and is similar in amorphous and crystalline SiO_2 (Skuja 1994, 1998; Fitting et al. 2001). The recombination of the so-called self-trapped exciton (STE) involves an irradiation-induced electron hole pair (oxygen Frenkel pair) consisting of an oxygen vacancy and a peroxy linkage (e.g., Stevens-Kalceff and Phillips 1995; Stevens-Kalceff 2009).

On the other hand, there are speculations about the role of Ti as an activator of this 440–450 nm CL in quartz. Several studies reported a correlation between the intensity of this luminescence and the concentration of Ti in quartz, with the brightest CL corresponding to the highest Ti concentrations (e.g., Müller et al. 2002, 2003; Van den Kerkhof et al. 2004; Rusk et al. 2008). First attempts were made to quantify the Ti concentration in quartz by using the intensity of the ~450 nm emission band (Leeman et al. 2012; Vasyukov et al. 2013).

However, up until now there has been no study combining a structure and spectroscopic investigation to determine that Ti is responsible for the activation of the blue ~450 nm (2.8 eV) emission in quartz.

The present study was aimed to elucidate the origin of the 440–450 nm (2.75–2.8 eV) CL emission in quartz by an analytical combination of scanning electron microscope (SEM) and optical microscope (OM) CL imaging and spectroscopy with defect structural analyses by EPR spectroscopy and trace element analyses by electron microprobe as well as inductively-coupled plasma mass spectrometry (ICP-MS). The CL analyses include a time-series of spectral measurements to test the stability of the luminescence related defects under the electron beam. This investigation of geologically well-defined samples and synthetic quartz from Ti-diffusion experiments proves the validity of blue luminescent quartz as an indicator for specific defects in quartz and related conditions of formation.

MATERIALS AND METHODS

Sample materials

The investigation materials comprise quartz samples from different geological environments and different trace-element compositions. The essential criterion for sample selection was the visible blue luminescence of quartz with an emission band at 440–450 nm. Both high-purity quartz (HPQ) with very low impurity contents (Ti concentrations < 5 ppm) and Ti-rich quartz from volcanic host rocks were analyzed. In addition, synthetic quartz samples from Ti-diffusion experiments were included, which consist of high-purity crystal cores (< 0.1 ppm Ti) and Ti-rich rims (Audétat et al. 2021). The specimens selected for the present study are compiled in Table 1. Some of the presented Ti concentrations and EPR data refer to analytical studies from earlier publications.

Titanium-rich quartz from volcanic host rocks is represented by quartz phenocrysts from two rhyolites of the NW-Saxonian Volcanic Complex (Germany). The sample Börtewitz

belongs to the Kemmlitz porphyry and the sample Hausdorf to the Leisnig porphyry (Götze et al. 2017a, 2020). In both rocks the quartz phenocrysts show bright blue CL (Fig. 1a,b) and Ti-related point defects were detected by EPR spectroscopy (Table 1). Whereas the quartz phenocrysts in the rhyolite from Börtewitz show only slight zoning, quartz crystals in the Hausdorf sample exhibit distinct growth zoning under CL.

Two massive pegmatite quartz samples are represented by a smoky quartz from the pegmatite field Li in the Evje-Iveland district (Norway) and a rose quartz from the Rubicon Mine in Namibia, respectively (Götze et al. 2004, 2005). The visible blue luminescence of these two quartz samples (Fig. 1c,d) is dominated by a transient broad band centered at ca. 500 nm, which also includes a stable ~450 nm component. Both quartz samples show elevated Ti contents and detectable $[TiO_4/Li^+]^0$ centers. Although the Ti content of the rose quartz from the Rubicon Mine is lower (13.6 ppm) than that of the smoky quartz from Li (25.2 ppm), Ti in the former seems to be completely incorporated into the quartz lattice, whereas additional mineral micro-inclusions of rutile were detected in the latter (Götze et al. 2004).

Two high-purity hydrothermal quartz samples derive from the locations Kyshtym and Kuznechikhinsk in the Ural region (Russia). Both samples have extremely low Ti contents and no structural Ti could be detected by EPR spectroscopy (Götze et al. 2017b). Nevertheless, both quartz samples exhibit an initial blue CL with a luminescence emission band at ~450 nm (Fig. 1e,f). The same behavior was observed for the high-purity metamorphic quartzite from Yurma (Ural, Russia – Fig. 1g). Again, no structural Ti was detectable (Götze et al. 2017b).

The last sample set of 8 quartz crystals derives from Ti-diffusion experiments with synthetic quartz (Audétat et al. 2021). Annealing experiments (1,000–1,600 °C, 1 atm to 2.0 GPa) were performed for 3–84 days on crystal-crystal diffusion couples consisting of almost Ti-free synthetic quartz seeds (< 0.1 ppm Ti) over which Ti-rich quartz (ca. 100–3,000 µg/g

This is the peer-reviewed, final accepted version for American Mineralogist, published by the Mineralogical Society of America.
The published version is subject to change. Cite as Authors (Year) Title. American Mineralogist, in press.
DOI: https://doi.org/10.2138/am-2022-8884. http://www.minsocam.org/

Ti) was grown hydrothermally. The sample set comprises both crystals from the original starting material (QTiDi-10 and QTiDi-35) and crystals after HT-diffusion experiments (QTiDi-22, 23, 24, 25, 26, 30). All crystals consist of Ti-poor cores and 50–300 µm thick Ti-rich rims, which exhibit blue CL with a dominant ~450 nm band (Fig. 1h).

Analytical methods

Polished thin sections were prepared for cathodoluminescence (CL) investigations from all quartz samples listed in Table 1. In addition, separate crystals of synthetic quartz from Ti-diffusion experiments were embedded in epoxy resin and prepared as polished mounts for SEM and microprobe measurements. Aliquots of the sample material were prepared as fine-grained powders for trace-element analysis and EPR spectroscopy, respectively.

Cathodoluminescence (CL). CL measurements were performed on carbon-coated thin sections, first using a hot-cathode CL microscope HC1-LM (Neuser et al. 1995). The system was operated at 14 kV and 0.2 mA with a defocused electron beam. Luminescence images were captured using a Peltier cooled digital video-camera (OLYMPUS DP72). CL spectra in the wavelength range 370 to 920 nm were recorded with an Acton Research SP-2356 digital triple-grating spectrograph with a Princeton Spec-10 charge-coupled device (CCD) detector that was attached to the CL microscope by a silica-glass optical fiber. CL spectra were measured under standardized conditions (wavelength calibration by an Hg-halogen lamp, spot width 30 µm, measuring time 5 s). Electron irradiation experiments were performed to measure the behavior of the quartz samples under electron bombardment. Samples were irradiated for up to 10 min under constant conditions (14 kV, 0.2 mA) and spectra were measured in time-series initially and after every 20 seconds, where the acquisition time was the sampling time.

In addition, hyperspectral CL data in the wavelength range 200 to 990 nm were collected on selected quartz grains by stage scanning of a 3.4 x 2.8 mm area (2-µm steps). The analyses were performed on a JEOL JXA 8500F electron microprobe analyser (EMPA) equipped with an integrated grating CL spectrometer and CCD detector at 20 kV accelerating voltage and 40 nA beam current (MacRae et al. 2009). For each measured pixel, wavelength dispersive X-ray data were simultaneously collected for Ti, Al, Fe, Mg, and Si by energy dispersive spectrometry. Complete spectral data were acquired for each pixel, allowing analysis and construction of spatial maps of all measured parameters. In detail, the CL spectra were deconvolved in energy space using Chimage software (Harrowfield et al. 1993; MacRae et al. 2013). Each of the resolved energy contributions could be mapped separately to resolve the spatial distribution of specific CL emissions. Cathodoluminescence spectra have been corrected for the optical response of the fiber and optical spectrometer.

Electron paramagnetic resonance (EPR). The measurement of single-crystal EPR spectra was not possible for most samples because of the limited sample material, and measurements were made with ~200 mg of pulverized materials for natural quartz samples and <50 mg for synthetic quartz. Only two large crystals from the synthetic quartz from Ti diffusion experiments (sample TiDi 35 as starting material with 2000-3000 ppm Ti and TiDi 24-11 as material after diffusion experiments) were used for single-crystal EPR measurements.

Analyses of the paramagnetic centers in quartz were performed using a Bruker EMX spectrometer operated with the X-band microwave frequencies at both room temperature and liquid-nitrogen temperature. Experimental conditions for room-temperature EPR included a microwave frequency of ~9.63 GHz, modulation frequency of 100 kHz, modulation amplitude of 0.1 mT, and microwave powers from 0.02 mW to 20 mW. The spectral resolutions were ~0.146 mT for wide scans 50–6500 mT and 0.024 mT for narrow scans 300–350 mT. After room-temperature EPR measurements all samples were irradiated in a ^{60}Co cell

for 72 days at a dose of ~104 kGy. Low-temperature (85 K) EPR measurements were made immediately after gamma-ray irradiation, with similar experimental conditions used for the room-temperature analyses except for a microwave frequency of ~9.39 GHz. Single-crystal EPR measurements in two approximately orthogonal planes were made at constant rotation intervals of 4° for one plane (i.e. approximately perpendicular to the xz plane, where the orthogonal experimental coordinate xyz with the z and x axes parallel to the crystallographic c- and a-axes, respectively, Mashkovtsev et al. 2013) and 5° for another one (i.e. approximately the yz plane), using the following conditions: scan range of 336-354 mT, microwave power of 2.1 mW, modulation frequency of 100 kHz, modulation amplitude of 0.1 mT, and spectral resolution of 0.01 mT.

Trace elements. Concentrations of trace elements in the samples of pegmatite quartz, hydrothermal quartz and the metamorphic quartzite were analyzed using solution ICP-MS. 400–500 mg sample materials were milled to a grain size of <30 μm using a pre-cleaned agate mortar. The powdered sample was digested in a glassy carbon vessel with 5 mL concentrated HF and 3 mL concentrated HNO_3 at 50 °C (35 min). Rhenium solution (1 mL of 100 μg L^{-1} concentration) was added as an internal standard for the ICP-MS measurements. The analyses were performed using a Perkin Elmer Sciex Elan 5000 quadrupole instrument with a cross-flow nebulizer and a rhyton spray chamber. The precision and accuracy of the ICP-MS measurements were evaluated by analysis of the glass sand reference material UNS-SpS. The relative standard deviations for most elements were below 10% (Monecke et al. 2000).

Trace element concentrations of Ti in the polished sections of volcanic quartz phenocrysts and the synthetic quartz samples from Ti-diffusion experiments were analyzed using wavelength dispersive spectrometry (WDS). Analyses were performed post CL mapping on a JEOL 8530F microprobe at 20 kV, 100 nA, with a 5 μm spot. Standards used were synthetic quartz for Si and rutile for Ti. CL spectra were extracted from the map corresponding to each analysed region and fitted for a non-bridging oxygen hole center

This is the peer-reviewed, final accepted version for American Mineralogist, published by the Mineralogical Society of America.
The published version is subject to change. Cite as Authors (Year) Title. American Mineralogist, in press.
DOI: https://doi.org/10.2138/am-2022-8884. http://www.minsocam.org/

(NBOHC – 1.89 eV) and Ti^{4+} peak (2.8 eV). The 2σ detection limit for quantitative Ti measurements was 16 ppm.

RESULTS

Quartz phenocrysts from rhyolites

The quartz phenocrysts in the rhyolite from *Börtewitz* (Saxony, Germany) exhibit a more or less homogeneous blue CL (compare Fig. 1a) and observed banding is not very strong. Spectral measurements show two dominating emission bands at 1.9 eV (650 nm; FWHM 0.43 eV) and 2.8 eV (445 nm; FWHM 0.91 eV) (Fig. 2a). Peak fitting of the spectra revealed a third subordinate emission band at 2.46 eV (505 nm; FWHM 0.65 eV). Different crystal areas show varying intensities of the individual peaks. The quantitative distribution of the two main CL emissions is shown in the monochromatic images in Figures 2b and c.

The map distribution of the intensities for the 1.9 eV and 2.8 eV resolved components provides information about the spatial distribution of different defects in quartz. The orange to red emission band at 1.9 eV (650 nm) is probably the most common CL emission in natural and synthetic quartz. This emission is attributed to the recombination of electrons in the nonbridging oxygen band-gap state with holes in the valence-band edge (Siegel and Marrone 1981). A number of different precursors of this nonbridging oxygen hole center (NBOHC) have been proposed resulting in slight varying band positions (Stevens Kalceff and Phillips 1995; Stevens Kalceff 2009). The intensities of this CL emission reflect the distribution of defects inherent to the quartz structure.

The distribution pattern of the 2.8 eV CL emission is opposite to that of the 1.9 eV emission (Fig. 2c). The comparison of the spatial intensity distribution of this CL emission with the analyzed Ti contents shows a positive correlation trend (Fig. 3b). Higher Ti concentrations result in higher intensities of the 2.8 eV CL emission. Therefore, the 2.8 eV

distribution map directly reflects the distribution of Ti in quartz. It is noted that the 2.8 eV versus Ti scatter plot in Figure 3b appears to show two distinct clusters. These do not correspond to the upper and lower grains (Fig. 3a), but are rather reflect the analysis point distribution. The low R^2 number reflects the fine zoning encountered in these grains. The structural incorporation of Ti into the quartz lattice is evidenced by results of EPR measurements, which show the presence of elevated contents of the $[TiO_4/Li^+]^0$ center in the volcanic quartz phenocrysts (Götze et al. 2017a, 2020).

Investigations of quartz phenocrysts in the rhyolite from *Hausdorf* (Saxony, Germany) provided similar results compared to those from Börtewitz. The quartz crystals exhibit a bluish-violet CL and distinct growth zoning (Fig. 1b). The CL spectra consist of two dominant emission bands in the red at 1.9 eV and blue at 2.8 eV (Fig. 4a) as well as a subordinate emission band at 2.46 eV. Depending on the absolute intensities there is a slight shift of the spectral position of the blue CL emission band. The CL heterogeneities of the quartz crystals are caused by intensity variations of the individual bands. Figures 4 b,c show monochromatic maps of the intensity distribution of the two main CL emissions at 1.9 and 2.8 eV, respectively.

Similar to the sample from Börtewitz, the intensities of the blue ~450 nm emission correlate with the analyzed Ti content in quartz (Fig. 5b) with the highest CL intensities corresponding to the highest Ti concentrations. In conclusion, the 2.8 eV CL distribution map (Fig. 4c) more or less directly reflects the distribution of Ti in quartz. The EPR detection of paramagnetic $[TiO_4/Li^+]^0$ centers in the quartz phenocrysts strongly supports the idea that the blue CL emission band at ~450 nm might be activated by Ti^{4+}.

Pegmatite quartz

The two pegmatite quartz samples from Li (Evje-Iveland, Norway) and the Rubicon Mine (Namibia) are also characterized by a visible blue CL (Figs. 1c,d). The CL spectra show

two main emission bands at 390 nm (3.15 eV) and 500 nm (2.45 eV), which have different intensity ratios in the two quartz samples (Fig. 6). The dominant CL is transient and disappears during prolonged electron irradiation and a weak stable emission band at ~450 nm remains.

The short-lived emissions at 390 and 500 nm can be related to alkali-compensated trace-element centers in the quartz structure (Ramseyer and Mullis 1990; Perny *et al.* 1992, Götze *et al.* 2005). It was proved that the CL emission band at ca. 390 nm (3.15 eV) correlates well with the Al content and the concentration of $[AlO_4/M^+]$ defect centers (Alonso *et al.* 1983; Luff and Townsend 1990; Perny *et al.* 1992). In addition, Ramseyer and Mullis (1990) and Perny *et al.* (1992) concluded that the CL emission at 500 nm (2.45 eV) can be related to the uptake of positively charged interstitial cations (Li^+, H^+, Na^+) associated with the substitution of Al for Si. Both transient CL emissions are sensitive to irradiation damage that can probably be attributed to the recombination of a hole trapped adjacent to a substitutional, charge-compensated center. The rapid attenuation of the CL emissions under the electron beam result from the dissociation and electromigration of the charge compensating cations out of the interaction volume (Perny et al. 1992).

These conclusions are supported by the trace element data and results of EPR measurements. The pegmatite quartz from Li contains 178 ppm Al and 24.1 ppm Li, and the quartz from the Rubicon Mine has 552 ppm Al and 84.5 ppm Li (Götze et al. 2004). The structural incorporation of these elements was evidenced by the EPR data, which show high contents of substitutional defect Al as a result of diamagnetic $[AlO_4/M^+]$ precursor defects that were transformed during irradiation into paramagnetic $[AlO_4]^0$ centers (Fig. 7).

In addition, the existence of $[TiO_4/Li^+]^0$ centers was detected in the EPR spectra (Fig. 7) confirming analyzed elevated concentrations of Ti in the pegmatite quartz (Li 25.2 ppm, Rubicon Mine 13.6 ppm). Therefore, the stable ~450 nm emission could probably be related to substitutional Ti^{4+} in quartz as supposed for the volcanic quartz phenocrysts. However, in

This is the peer-reviewed, final accepted version for American Mineralogist, published by the Mineralogical Society of America.
The published version is subject to change. Cite as Authors (Year) Title. American Mineralogist, in press.
DOI: https://doi.org/10.2138/am-2022-8884. http://www.minsocam.org/

the pegmatite quartz the ~450 nm emission is only visible after electron irradiation due to the decreasing intensities of the two dominating emission bands, which initially covered this band.

High-purity hydrothermal and metamorphic quartz

The group of high-purity quartz (HPQ) comprises two hydrothermal quartz samples and one metamorphic quartz sample (Table 1). All selected quartz samples have extremely low Ti contents between 2.74 and 4.54 ppm and no structural Ti could be detected by EPR spectroscopy (Götze et al. 2017b). The HPQ quartz samples show a very similar luminescence behavior and exhibit an initial blue CL with a luminescence emission band at ~450 nm (Figs. 1e–g, Fig. 8).

However, the interaction with the electron beam resulted in significant changes of the CL emission. Figure 8b illustrates a nearly exponential decrease of the intensity of the ~450 nm CL emission band. The 650 nm emission is also sensitive to electron irradiation. The increase of this emission band during electron irradiation results from the transformation of precursor centers into NBOHC under the electron beam (Ramseyer et al.1988; Götze et al. 2001).

The hydrothermal HPQ from Kuznechikhinsk and the metamorphic high-purity quartz from Yurma exhibit an almost identical luminescence behavior compared to that of the Kyshtym quartz (Fig. 9). Both have an initial visible blue CL with a strong emission band at ~450 nm. The CL emission intensity is not stable under the electron beam and the ~450 nm band intensity strongly decreases, whereas the 650 nm band slightly increases. The lack of structural Ti and the detection of E'_1 centers proved by EPR measurements (Götze et al. 2017b) indicate that the blue CL at ~450 nm cannot be associated with trace Ti, but must be related to structural defects.

Synthetic Ti-rich quartz

The sample set of synthetic quartz comprises crystals consisting of Ti-poor synthetic quartz seeds (< 0.1 ppm Ti) over which 50–300 μm thick Ti-rich quartz rims were grown hydrothermally. Besides these original samples, quartz crystals were investigated that additionally underwent high-temperature diffusion experiments. For both types of synthetic quartz, differences in the chemical composition are clearly reflected in the CL properties of the crystals (Figs. 1h, 10).

The comparison of the CL image (Fig. 10a) with the local spectral CL measurements in Figure 10b provides information about the distribution of the defects responsible for the 1.9 eV and 2.8 eV components, the latter of which directly reflects the distribution of Ti. In particular, it can be seen that the intensity of the 1.9 eV emission is quite low indicating relatively uniform CL contributions inherent to the quartz structure (non-bridging oxygen hole center – NBOHC). In contrast, the CL image clearly illustrates the distinctive overgrowth of Ti-rich quartz on the Ti-poor core with an inner bright zone (higher Ti content) followed by an outer zone with less intensity and lower Ti content (Fig. 10).

The fitted intensities of the 2.8 eV CL emissions versus Ti concentration in Figure 11 provide no strong correlation but a clear trend with higher intensities related to higher Ti contents. The Ti concentrations in the quartz diffusion rim vary in a range from 2000 to 3750 ppm. However, it appears that nano-rutile could also be detected, i.e., not all Ti seems to be structurally incorporated in the quartz crystal.

An interesting aspect of the CL properties was revealed by additional time-series CL measurements. The results show that both the crystal core and rim exhibit an initial blue CL with different intensities (Fig. 12). The initial CL of the Ti-poor crystal core is dark blue and shows a ~450 nm emission band. This band quickly disappears under the electron beam and after less than 60 s the red 650 nm band (NBOHC) becomes dominant (Fig. 12b). This might

be the reason, why the ~450 nm emission was not detectable in the SEM-CL mappings, where it already disappeared due to the prolonged electron irradiation.

In contrast, the Ti-rich diffusion rim shows a bright blue CL with intensities of more than tenfold of that from the primary hydrothermal quartz seed. The emission band appears at the same position at ca. 450 nm (2.8 eV), but this one is more or less stable even after several minutes of electron irradiation (Fig. 12b). These results illustrate that two different types of CL emission at the same spectral position appear in the quartz crystals. The differentiation of these two emission bands is possible by both time-series measurements and by collecting spectral CL maps and using fitted peaks to differentiate the different peak widths of the STE emission versus the Ti^{4+} centers. The damage measurements show the initial emission and the behavior under the electron beam, accompanied by chemical analyses of the Ti content in the different areas. The STE peak appears to be consistently broader compared to the Ti^{4+} peak as can be seen in Figure 13. In general, the STE peak has a full width half maximum (FWHM) of 1.08–1.26 eV while the Ti^{4+} FWHM is 0.87–0.95 eV.

Figure 14 is a powder EPR spectrum measured at 30 K after prolonged γ-irradiation of the original Ti-rich quartz (TiDi-35) used as the starting material for the diffusion experiments. The spectrum shows at least 4 distinct centers, 3 well established ones ($[AlO_4]^0$, E'_1 and $[TiO_4/H]^0$) and an unknown one. The unknown axial center with $g_{//}$=1.943 and $g_{\perp}$=1.977) is tentatively labeled as $[TiO_3]^-$ or Ti E'_1 (i.e. a Ti analogue of the well-known E'_1 center, Mashkovtsev et al. 2013). The ^{47}Ti hyperfine sextet appears to be visible in the spectrum measured at 10 dB. This new oxygen-vacancy electron center probably arises from an oxygen vacancy next to a substitutional Ti^{4+} ion (i.e., a 3-fold coordinated Ti atom; Mashkovtsev et al. 2013) and is most likely generated at high temperature and pressure required to drive Ti into the quartz structure.

The powder EPR spectrum of the titanium diffused quartz (Figure 15) is clearly different from that of the starting material (TiDi-35), with only two centers ($[AlO_4]^0$ and

This is the peer-reviewed, final accepted version for American Mineralogist, published by the Mineralogical Society of America.
The published version is subject to change. Cite as Authors (Year) Title. American Mineralogist, in press.
DOI: https://doi.org/10.2138/am-2022-8884. http://www.minsocam.org/

$[TiO_4]^-$). The unknown Ti-related center is now absent. Moreover, the pronounced E'_1 center in TiDi-35 is conspicuously absent as well. The disappearance of the latter two defects suggests that oxygen vacancies present in the as-grown samples were completely eliminated during the high-T diffusion experiments. Moreover, during the HT diffusion experiments the kind of Ti-defects changes and the $[TiO_4/H]^0$ center transformed into the $[TiO_4]^-$center. Hydrogen was probably lost after high-T diffusion and, therefore, not available for the formation of the $[TiO_4/H]^0$ center (Rinneberg and Weil, 1972), which is present in the original sample (Fig. 14) but not detected in the diffused sample (Fig. 15).

Although the EPR measurements do not allow the differentiation between rim and core areas of the quartz crystals, the Ti contents of the Ti-rich overgrowths are high enough to be detected even though the volume of these thin rims is minimal relative to the overall sample size. Accordingly, the structural incorporation of Ti^{4+} into the quartz rims was proved, which is obviously responsible for the observed blue luminescence.

DISCUSSION

Origin of the ~450 nm blue CL in quartz

The present study confirms previous results that the cathodoluminescence of quartz is highly variable depending on the specific physico-chemical environment (Ramseyer et al. 1988; Götze et al. 2001; Stevens-Kalceff 2009). In particular in the spectral range between 2.3 and 3.3 eV multiple overlapping spectral components exist, which are associated with various intrinsic and extrinsic defects (compare Fig. 6). Gorton et al. (1997), for instance, found at least four different luminescence bands with maxima at 390, 420, 450 and 500 nm using a phase-tuning technique. The specific band positions may vary in dependence on the genetic conditions of formation, experimental conditions as well as the number and intensity of the individual luminescence emissions present (e.g., Walker 1985; Luff and Townsend 1990;

Stevens-Kalceff 2009). This shift of the band position was also observed in the present study for the blue band at 440–450 nm (2.75–2.8 eV).

The results of the study revealed that certain high-purity quartz samples with extremely low trace-element contents (in particular Ti) exhibit the blue CL emission band at ~450 nm (Figs. 8, 9, 12c). Several studies on natural and synthetic samples evidenced that the blue CL emission at ~450 nm in quartz is associated with the recombination of the self-trapped exciton (STE) related to oxygen vacancies (Stevens-Kalceff and Phillips 1995; Skuja 1998; Stevens-Kalceff 2009). This native defect center occurs when excitons (i.e., excited electron-hole pairs) create a localized self-induced lattice distortion in the normally ideal crystal lattice that traps the exciton ($\equiv O_3–Si\bullet\ \bullet Si–O_3\equiv$). The radiative relaxation of the STE after excitation with an electron beam produces a broad luminescence band and results in the restoration of the former defect free lattice configuration (Skuja 2000). This behavior can explain the observed decrease of the 450 nm STE-emission under the electron beam (Figs. 8, 9, 12c).

The relation of the ~450 nm CL emission to oxygen vacancies in quartz was previously confirmed by experimental studies (Barfels 2001; Salh et al. 2007). Cathodoluminescence spectra of pure SiO_2 samples and those implanted by silicon ($SiO_{<2}$) show a significant increase of the 450 nm emission due to the creation of oxygen deficient centers (ODC), whereas oxygen implantation ($SiO_{>2}$) resulted in an increase of the 650 nm CL emission band (formation of NBOHC). The detection of E'_1 centers by EPR in the investigated quartz samples proved the existence of oxygen vacancies. Although the E'_1 center alone is paramagnetic and not luminescent, defect pairs such as an *E*‘ center with interstitial oxygen or NBOHC can act as possible exciton candidates for STE in silica polymorphs (Fisher et al. 1990).

In addition to the ~~evidenced~~ activation of the 450 nm band by structural defects, the present study also provides new indications concerning the possible role of Ti as an activator

of blue CL in quartz. Some previous studies suggested a correlation between the intensity of blue luminescence and the concentration of Ti in quartz, with the brightest CL corresponding to the highest Ti concentrations (e.g., Müller et al. 2002, 2003; Van den Kerkhof et al. 2004; Rusk et al. 2008; Leeman et al. 2012; Drivenes et al. 2016). However, up to now the spectroscopic evidence concerning the activation of the 450 nm emission in quartz by Ti was missing.

In the present study, structural Ti^{4+} at the Si^{4+} position in the tetrahedron was indeed detected by EPR in Ti-bearing quartz crystals of different origins, causing a blue CL band at ~450 nm in these samples. In particular, in quartz phenocrysts of rhyolites as well as synthetic quartz with varying Ti contents, there was a tendency for higher Ti contents to increase the intensity of the ~450 nm emission band (Figs. 3, 5, 11). In contrast, in quartz samples with different CL activators, the ~450 nm band was partially overlaid by other emission bands, so that this band became visible only after the dominant emissions had decayed (Fig. 6). Accordingly, as Ti content in quartz decreases, other energy peaks become increasingly prominent. In case that both types of defects (STE + Ti^{4+}) responsible for the ~450 nm CL emission are present in the quartz crystal, it is extremely difficult to distinguish between intrinsic and extrinsic defects and associated emission components based purely on their relative peak positions. A determination on the type of emission centers can be made through the combined use of EPR spectroscopy, trace element analysis, hyperspectral CL mapping and peak fitting together with time-series CL spectroscopy. The latter two techniques, hyperspectral CL analysis and time-series CL, are most likely to be the easiest for most research groups.

Quantitative aspects of Ti-activated CL in quartz

In addition to the general discussion of the role of structurally incorporated Ti^{4+} as a luminescence activator in quartz, various attempts have been made to quantify Ti contents in

quartz based on CL intensities. In particular, bulk luminescence intensities from panchromatic SEM-CL images ("grayscale" intensities) have been correlated with absolute Ti contents (e.g., Müller et al. 2003; Landtwing and Pettke 2005; Rusk et al. 2006, 2008, Matthews et al. 2012). However, such correlations of trace element contents with the overall visible luminescence intensities are not meaningful because in most samples the total luminescence intensity is composed of multiple emission bands from different defects. Moreover, many CL emissions in quartz are linked to intrinsic lattice defects and not to trace elements. For this reason, total CL intensities cannot be expected to vary linearly with the content of Ti or other trace elements. Although the Ti-related CL emission band at 2.8 eV in quartz phenocrysts in rhyolites might be the dominant CL emission, the issue is critical with regard to titanium diffusion chronology applications in which time scales are estimated from grayscale profiles in panchromatic CL images (e.g., Wark and Watson 2007; Matthews et al. 2012; Chamberlain et al. 2014; Cooper et al. 2017).

Following the development of hyperspectral CL mapping together with peak fitting supported by trace element analysis undertaken in either an EPMA (Leeman et al. 2012) or Laser Ablation Inductively Coupled Mass Spectroscopy (MacRae et al. 2009) it has been demonstrated that this approach allows a range of emission centers from REE^{3+} to Ti^{4+} to be correlated with elemental abundancies. The present investigation has confirmed that only by means of CL spectroscopy in combination with EPR measurements and trace element analyses an assignment of defects and thus a rigorous quantification of specific trace elements is possible. Thereby, the comparison of the specific trace element content with the intensity of an individual luminescence band could be significant. Nevertheless, the demonstrated correlations of the intensities of the ~450 nm emission band with the local trace Ti contents have shown that even in this case there are clear trends, but no straight linear correlations exist (Figs. 3, 5, 11).

This is the peer-reviewed, final accepted version for American Mineralogist, published by the Mineralogical Society of America.
The published version is subject to change. Cite as Authors (Year) Title. American Mineralogist, in press.
DOI: https://doi.org/10.2138/am-2022-8884. http://www.minsocam.org/

~~The main reason for the uncertainties in the specific case of the ~450 nm band is that an intrinsic defect (STE) can cause luminescence in the same spectral region. Thus, a blue CL emission band at ~ 450 nm (2.8 eV) can also occur in ultrapure quartz without any Ti impurities. Differentiation of the defects was possible analyzing CL measurements in a time-series and EPR analyses.~~

In the synthetic quartz samples from Ti diffusion experiments, the Ti content was sometimes so high that not all Ti could be structurally incorporated as Ti^{4+}, but elemental Ti could also be detected (that is not available for luminescence activation). The same will happen in natural quartz, if part of the Ti is incorporated as TiO_2 micro-inclusions, as in the case of the pegmatite quartz samples (compare Götze et al. 2004). In addition, correlative relations between the CL and single trace elements are very difficult due to the complexity of the luminescence process hampering a clear quantitative evaluation of the CL spectra (e.g. processes of sensitizing and quenching; Habermann 2002; Götze 2012). Therefore, a very complex approach is necessary for the accurate elucidation and possible quantification of luminescence processes.

IMPLICATIONS

The present study was aimed to elucidate the origin of the ~450 nm (2.8 eV) CL emission in quartz and to find possible quantitative relations to the structural incorporation of Ti. The investigation of quartz of different origin and containing different concentrations of Ti revealed that both structural defects not related to trace elements (self-trapped exciton – STE) and also incorporation of Ti^{4+} into the quartz structure can activate the blue CL emission at the same wavelength position. The STE-activated CL emission is highly sensitive to electron beam damage and is most often detectable in quartz when the Ti content is relatively low (e.g., high-purity hydrothermal and metamorphic quartz), whereas high Ti concentrations

from tens to hundreds of ppm result in a stable blue CL emission. However, both CL emissions can also occur simultaneously in one quartz crystal.

The common activation of the ~450 nm luminescence emission in quartz by an intrinsic defect (STE related to oxygen vacancy) and structurally incorporated Ti^{4+} as additional activator prevents a serious quantitative evaluation of the CL signal. A reliable distinction of the two different CL emissions at ~450 nm is only possible by time-series CL spectroscopy combined with EPR spectroscopy and trace-element analysis of the Ti concentration. This finding is especially interesting with regard to correlations of trace-element contents and CL intensities, in particular with panchromatic SEM-CL investigations. Our results illustrate, that blue CL emission at ~450 nm can even appear in high-purity quartz with very low trace element contents.

Acknowledgments

We thank Eli Wiens for collecting all EPR spectra and Rudolf Mashkovtsev for discussions on EPR results. We also thank Cameron Davidson (CSIRO Minerals Resources Clayton, Australia) for preparing several of the polished mounts examined in this study. The authors gratefully acknowledge funding from Australian Research Council (ARC) LE130100087. The reviews of two anonymous reviewers improved the quality of the paper. Editorial handling of Andreas Ertl is gratefully acknowledged.

REFERENCES CITED

Alonso, P.J., Halliburton, L.E., Kohnke, E.E., and Bossoli, R.B. (1983) X-ray induced luminescence in crystalline SiO_2. Journal of Applied Physics, 54, 5369–5375.

Audétat, A., Miyajima, N., Wiesner, D., and Audinot, J.-N. (2021) Confirmation of slow Ti diffusion in quartz by diffusion couple experiments and evidence from natural samples. Geology, 49, 963–967.

Barfels, T. (2001) Kathodolumineszenz amorpher und kristalliner Modifikationen von SiO_2 and GeO_2, 168 pp. Ph.D. thesis, Rostock University, Germany.

Cerin, D., Götze, J., and Pan, Y. (2017) Radiation induced damage in quartz at the Arrow uranium deposit, southwestern Athabasca Basin, Saskatchewan. Canadian Mineralogist, 55, 457-472.

Chamberlain, K.J., Morgan, D.J. and Wilson C.J.N. (2014) Timescales of mixing and mobilisation in the Bishop Tuff magma body: perspectives from diffusion chronometry. Contributions to Mineralogy and Petrology, 168, 1034. doi.org/10.1007/s00410-014-1034-2

Cooper, G.F., Morgan, D.J. and Wilson, C.J.N. (2017) Rapid assembly and rejuvenation of a large silicic magmatic system: Insights from mineral diffusive profiles in the Kidnappers and Rocky Hill deposits, New Zealand. Earth and Planetary Science Letters, 473, 1–13.

Fisher, A.J., Hayes, W., Stoneham, A.M. (1990) Structure of the self-trapped exciton in quartz. Physical Review Letters, 64, 2667–2670.

Fitting, H.-J., Barfels, T., Trukhin, A.N., Schmidt, B. (2001) Cathodoluminescence of crystalline and amorphous SiO_2 and GeO_2. Journal of Non-crystalline Solids, 279, 51–59.

Drivenes, K., Larsen, R.B., Müller, A., and Sørensen, B.E. (2016) Crystallization and uplift path of late Variscan granites evidenced by quartz chemistry and fluid inclusions: Example from the Land‘s End granite, SW England. Lithos, 252–253, 57 ‑ 75.

Gorton, N.T., Walker, G., Burley, S.D. (1997) Experimental analysis of the composite blue CL emission in quartz. Journal of Luminescence, 72–74, 669–671.

Götte, T., Pettke, T., Ramseyer, K., Koch-Müller, M., and Mullis, J. (2011) Cathodoluminescence properties and trace element signature of hydrothermal quartz: A fingerprint of growth dynamics. American Mineralogist, 96, 802–813.

Götze, J. (2009) Chemistry, textures and physical properties of quartz – geological interpretation and technical application. Mineralogical Magazine, 73, 645–671.

Götze, J. (2012) Application of cathodoluminescence (CL) microscopy and spectroscopy in geosciences. Microscopy and Microanalysis, 18, 1270–1284.

Götze, J. and Hanchar, J. (2018) Atlas of cathodoluminescence (CL) microtextures. GAC Miscellaneous Publication No. 10. Geological Association of Canada, St. John's, Newfoundland and Labrador, Canada, 248 pp.

Götze, J., Plötze, M., and Habermann, D. (2001) Cathodoluminescence (CL) of quartz: origin, spectral characteristics and practical applications. Mineralogy and Petrology, 71, 225–250.

Götze, J., Plötze, M., Graupner, T., Hallbauer, D.K., and Bray, C. (2004) Trace element incorporation into quartz: a combined study by ICP-MS, electron spin resonance, cathodoluminescence, capillary ion analysis and gas chromatography. Geochimica et Cosmochimica Acta, 6, 3741–3759.

Götze, J., Plötze, M., and Trautmann, T. (2005) Structure and luminescence characteristics of quartz from pegmatites. American Mineralogist, 90, 13–21.

Götze, J., Hanchar, J., Schertl, H.-P., Neuser, D.K., and Kempe U. (2013) Optical microscope-cathodoluminescence (OM–CL) imaging as a powerful tool to reveal internal textures of minerals. Mineralogy and Petrology, 107, 373–392.

Götze, J., Pan, Y., Stevens-Kalceff, M., Kempe, U., and Müller, A. (2015) Origin and significance of the yellow cathodoluminescence (CL) of quartz. American Mineralogist, 100, 1469–1482.

Götze, J., Lessig, F., Möckel, R., and Georgi, U. (2017a) Zur Mineralogie von Vulkaniten im Bereich des Kemmlitzer Porphyrs (Oschatz Formation, Nordwestsächsisches Becken). Veröffentlichung Museum für Naturkunde Chemnitz, 40, 77–94.

Götze, J., Pan, Y., Müller, A., Kotova, E.L., and Cerin, D. (2017b) Trace element compositions and defect structures of high-purity quartz from the Southern Ural region, Russia. Minerals, 7, 189. doi.org/10.3390/min7100189

Götze, J., Möckel, R., Breitkreuz, C., Georgi, U., and Klein, A. (2020) Zur Mineralogie von Vulkaniten und Lithophysen im Bereich des unterpermischen Leisniger Porphyrs (Nordwestsächsisches Becken). Veröffentlichungen Museum für Naturkunde Chemnitz, 43, 5–44.

Götze, J., Pan, Y., and Müller, A. (2021) Mineralogy and mineral chemistry of quartz – a review. Mineralogical Magazine, 85, 639-664.

Habermann, D. (2002) Quantitative cathodoluminescence (CL) spectroscopy of minerals: possibilities and limitations. Mineralogy and Petrology, 76, 247–259.

Harrowfield, I.R., MacRae, C., and Wilson, N.C. (1993) Chemical imaging in electron microprobes. In: Proceedings of the 27th Annual MAS Meeting 1993, Microbeam Analysis Society, New York, 547–548.

Jourdan, A.-L., Vennemann, T.W., Mullis, J., Ramseyer, K., and Spiers, C.J. (2009) Evidence of growth and sector zoning in hydrothermal quartz from Alpine veins. European Journal of Mineralogy, 21, 219–231.

Krickl, R., Nasdala, L., Götze, J., Grambole, D., and Wirth, R. (2008) Alteration of SiO_2 caused by natural and artificial alpha-irradiation. European Journal of Mineralogy, 20, 517–522.

Landtwing, M. and Pettke, T. (2005) Relationships between SEM-cathodoluminescence response and trace-element composition of hydrothermal vein quartz. American Mineralogist, 90, 122-131.

Leeman, W.P., McRae, C.M., Wilson, N.C., Torpy, A., Lee, C.-T.A., Student, J.J., Thomas, J.B., and Vicenzi E.P. (2012) A study of cathodoluminescence and trace element compositional zoning in natural quartz from volcanic rocks: Mapping titanium content in quartz. Microscopy and Microanalysis, 18, 1322–1341.

Lehmann, K., Pettke, T., and Ramseyer, K. (2011) Significance of trace elements in syntaxial quartz cement, Haushi Group sandstones, Sultanate of Oman. Chemical Geology, 280, 47–57.

Luff, B.J. and Townsend, P.D. (1990) Cathodoluminescence of synthetic quartz. Journal Physics Condensed Matter, 2, 8089–8097.

Mashkovtsev, R.I., Li, Z., Mao, M., and Pan, Y. (2013) ^{73}Ge, ^{17}O and ^{29}Si hyperfine interactions of the Ge E'_1 center in crystalline SiO_2. Journal of Magnetic Resonance, 233, 7–16.

Matthews, N.E., Huber, C., Pyle, D.M. and Smith, V.C. (2012) Timescales of magma recharge and reactivation of large silicic systems from Ti diffusion in quartz. Journal of Petrology, 53, 1385–1416.

MacRae, C.M., Wilson, N.C., and Brugger, J. (2009) Quantitative cathodoluminescence mapping with application to a Kalgoorlie Scheelite. Microscopy and Microanalysis, 15, 222–230.

MacRae, C.M., Wilson, N.C., and Torpy, A. (2013) Hyperspectral cathodoluminescence. Mineralogy and Petrology, 107, 429–440.

Monecke, T., Bombach, G., Klemm, W., Kempe, U., Götze, J., and Wolf, D. (2000) Determination of trace elements in the quartz reference material UNS-SpS and in natural quartz samples by ICP-MS. Geostandard Newsletter, 24, 73–81.

Müller, A., Kronz A., and Breiter K. (2002) Trace elements and growth patterns in quartz: a fingerprint of the evolution of the subvolcanic Podlesi granite system (Krušné Hory, Czech Republic). Bulletin of the Czech Geological Survey, 77, 135–145.

Müller, A., Wiedenbeck, M., Van den Kerkhof, A.M., Kronz, A., and Simon K. (2003) Trace elements in quartz – a combined electron microprobe, secondary ion mass spectrometry, laser-ablation ICP-MS, and cathodoluminescence study. European Journal of Mineralogy, 15, 747–763.

Müller, A., Breiter, K., Seltmann, R. and Pécskay, Z. (2005) Quartz and feldspar zoning in the eastern Erzgebirge volcano-plutonic complex (Germany, Czech Republic): evidence of multiple magma mixing. Lithos, 80, 201-227.

Neuser, R.D., Bruhn, F., Götze, J., Habermann, D., and Richter, D.K. (1995) Kathodolumineszenz: Methodik und Anwendung. Zentralblatt Geologie Paläontologie Teil I, H 1, 287–306.

Perny, B., Eberhardt, P., Ramseyer, K., and Mullis, J. (1992) Microdistribution of aluminium, lithium and sodium in quartz: Possible causes and correlation with short-lived cathodoluminescence. American Mineralogist, 77, 534–544.

Ramseyer, K., and Mullis, J. (1990) Factors influencing short-lived blue cathodoluminescence of alpha quartz. American Mineralogist, 75, 791–800.

Ramseyer, K., Baumann, J., Matter, A., and Mullis, J. (1988) Cathodoluminescence colours of alpha-quartz. Mineralogical Magazine, 52, 669–677.

Rinneberg H. and Weil, J.A. (1972) EPR Studies of Ti^{3+}-H^{+} centers in X-irradiated alpha-quartz. Journal of Chemical Physics, 56, 2019–2028.

Rusk, B.G., Reed, M.H., Dilles, J.H., and Kent, A.J.R. (2006) Intensity of quartz cathodoluminescence and trace-element content in quartz from the porphyry copper deposit at Butte, Montana. American Mineralogist, 91, 1300–1312.

Rusk, B., Lowers, H.A., and Reed M.H. (2008) Trace elements in hydrothermal quartz: Relationships to cathodoluminescent textures and insights into vein formation. Geology, 36, 547–550.

Salh, R., Fitting Kourkoutis, L., Schmidt, B., Fitting, H.-J. (2007) Luminescence of isoelectronically ion-implanted SiO_2 layers. Physica status solidi, 204, 3132–3144.

Siegel, G.H., and Marrone, M.J. (1981) Photoluminescence in as-drawn and irradiated silica optical fibers: an assessment of the role of nonbridging oxygen defect centres. Journal of Non-Crystalline Solids, 45, 235–247.

SivaRamaiah G., Lin J., and Pan Y. (2011) Electron paramagnetic resonance spectroscopy of Fe^{3+} ions in amethyst: Thermodynamic potentials and magnetic susceptibility. Physics and Chemistry of Minerals, 38, 159–167.

Skuja, L. (1994) Direct singlet-to-triplet optical absorption and luminescence excitation band of the twofold-coordinated silicon center in oxygen-deficient glassy SiO_2. Journal of Non-Crystalline Solids, 167, 229–238.

Skuja, L. (1998) Optically active oxygen-deficiency-related centers in amorphous silicon dioxid. Journal of Non-Crystalline Solids, 239, 16–48.

Skuja, . (2000) Optical properties of defects in silica. In: Pacchioni, G., Skuja, L., Griscom, D.L. (editors) Defects in SiO_2 and related dielectrics: Science and technology,. Kluwer, Dordrecht, The Netherlands, 387–392.

Stevens-Kalceff, M.A. (2009) Cathodoluminescence microcharacterization of point defects in α-quartz. Mineralogical Magazine, 73, 585–606.

Stevens-Kalceff, M.A. and Phillips, M.R. (1995) Cathodoluminescence microcharacterization of the defect structure of quartz. Physical Reviews B, 52, 3122–3134.

Van den Kerkhof, A.M., Kronz, A., Simon, K., Scherer, T. (2004) Fluid-controlled quartz recovery in granulite as revealed by cathodoluminescence and trace element analysis (Bamble sector, Norway). Contributions to Mineralogy and Petrology, 146, 637–652.

Vasyukov, O.V., Goemann, K., Kamenetsky, V.S., MacRae, C.M., and Wilson, N.C. (2013) Cathodoluminescence properties of quartz eyes from porphyry-type deposits: Implications for the origin of quartz. American Mineralogist, 98, 98–109.

Wark, D.A., Hildreth, W., Spear, F.S., Cherniak, D.J. and Watson, E.B. (2007) Pre-eruption recharge of the Bishop magma system. Geology, 35, 235–238.

Watt, G.R., Wright, P., Galloway, S., and McLean, C. (1997) Cathodoluminescence and trace element zoning in quartz phenocrysts and xenocrysts. Geochimica et Cosmochimica Acta, 61, 4337–4348.

Zinkernagel, U. (1978) Cathodoluminescence of quartz and its application to sandstone petrology. Contributions to Sedimentology, 8, 1–69.

This is the peer-reviewed, final accepted version for American Mineralogist, published by the Mineralogical Society of America.
The published version is subject to change. Cite as Authors (Year) Title. American Mineralogist, in press.
DOI: https://doi.org/10.2138/am-2022-8884. http://www.minsocam.org/

FIGURE CAPTIONS

Figure 1. CL micrographs of quartz samples investigated in the present study; (**a**) quartz phenocrysts in a rhyolite from Börtewitz (Saxony, Germany); (**b**) large quartz phenocryst in a rhyolite from Hausdorf (Saxony, Germany) showing distinct growth zoning; (**c**) massive pegmatite quartz from Li (Evje Iveland, Norway); the dark areas mark fluid trails and the arrow points to a micro-inclusion with radiation halo; (**d**) rose quartz from the Rubicon Mine (Namibia); the bright spots in the homogeneous crystal are related to areas with higher Al and Li contents; (**e/f**) high-purity hydrothermal quartz from Kyshtym and Kuznechikhinsk, respectively (Ural, Russia); subgrains are visible due to differing luminescence intensities, probably as a result of orientation dependence; (**g**) quartzite sample from Yurma (Ural, Russia); subgrain-boundaries are visible in CL; (**h**) synthetic Ti-poor hydrothermal quartz with Ti-rich rim (sample QTiDi-10) from diffusion experiments showing bright blue CL (note that the blue CL of the hydrothermal quartz center appears dark due to the short exposure time).

Figure 2. (**a**) CL spectra of different regions in the quartz phenocrysts from Börtewitz (compare Fig. 1a); the spectra show variations in the intensity ratios of the main peaks at 1.9 eV (NBOHC) and 2.8 eV; the numbers relate to the analytical spots (see Fig. 2c); (**b/c**) fitted intensity maps of CL showing the spatial intensity distribution of the 1.9 eV and 2.8 eV emissions, respectively; note the opposite distribution of the defects responsible for these two CL emission bands; the distribution map of the 2.8 eV CL emission directly reflects the distribution of Ti (compare Fig. 3b).

Figure 3. (**a**) Summed spectral CL map showing two quartz phenocrysts in the rhyolite from Börtewitz (Saxony, Germany) with the analytical points for Ti measurements; (**b**) plot of the

intensities of the fitted 2.8 eV CL emission band vs. analyzed Ti concentrations showing a positive correlation trend.

Figure 4. (**a**) CL spectra of different regions in the quartz phenocryst from Hausdorf (compare Fig. 1b); the spectra show variations in the intensity ratios of the main peaks at 1.9 eV (NBOHC) and 2.8 eV; the numbers relate to the analytical spots (see Fig. 4c); (**b**/**c**) fitted intensity maps of CL peaks showing the spatial intensity distribution of the 1.9 eV and 2.8 eV emissions, respectively; note the opposite distribution of the defects responsible for these two CL emission bands.

Figure 5. (**a**) Summed spectral CL map of a quartz phenocrysts in the rhyolite from Hausdorf (Saxony, Germany) with the analytical points for Ti measurements; (**b**) correlation of the 2.8 eV CL emission intensities and the analyzed Ti contents.

Figure 6. CL emission spectra of pegmatite quartz from Li (Evje-Iveland, Norway - **a**) and the Rubicon Mine, Namibia (**b**) showing initial strong bands at 390 (3.18 eV) and 500 nm (2.45 eV) with different band intensities; the intensities of the dominant emission bands strongly decrease during electron irradiation and a stable component at ~450 nm becomes visible.

Figure 7. EPR spectrum of pegmatite quartz from Li (Evje-Iveland, Norway) analyzed at 70K and 9.476 GHz in comparison with simulated spectra showing the dominance of $[AlO_4]^0$ and $[TiO_4/Li^+]^0$ centers.

Figure 8. (**a**) Fitted 2.8 eV intensity map of hydrothermal high-purity quartz from Kyshtym (Ural) showing the variable distribution of the ~450 nm emission; the variations of the CL

This is the peer-reviewed, final accepted version for American Mineralogist, published by the Mineralogical Society of America.
The published version is subject to change. Cite as Authors (Year) Title. American Mineralogist, in press.
DOI: https://doi.org/10.2138/am-2022-8884. http://www.minsocam.org/

intensity of the sub-grains probably result from the different crystallographic orientations causing different interactions with the electron beam; (**b**) CL spectra of the quartz from Kyshtym initially and after 300 s of electron irradiation illustrating the strong decrease of the ~450 nm emission intensity due to electron irradiation (see inset), whereas the 650 nm band (NBOHC) slightly increases.

Figure 9. Time-dependent CL spectra of the hydrothermal HPQ from Kuznechikhinsk (**a**) and the metamorphic high-purity quartz from Yurma; the spectra after 300 s of electron irradiation show a strong decrease of the initially dominating 450 nm CL emission band and a slight increase of the 650 nm emission (NBOHC).

Figure 10. (**a**) SEM-CL micrograph showing a synthetic quartz crystal after HT Ti-diffusion experiments with Ti-poor core (< 0.1 ppm Ti) and Ti-rich rim (2,000-3,000 ppm Ti); note the bright inner and darker outer zone of the rim; the numbers mark the analytical spots for spectral measurements; (**b**) CL spectra of the different areas in the analyzed quartz crystal; the core is dominated by the 650 nm (1.9 eV) CL emission (NBOHC), whereas the rim shows a strong emission band at 450 nm.

Figure 11. Plot of the intensities of the 2.8 eV CL emission band vs. analyzed Ti concentrations in seven samples of Ti-diffusion experiments showing a positive correlation trend (the analytical error is within the size of the symbols); ("dull CL" and "bright CL" in the sample designation relate to the visual CL intensity).

Figure 12. (**a/b**) CL images of synthetic hydrothermal quartz from Ti-diffusion experiments initially and after 180 s of electron irradiation; the primary Ti-poor center exhibits a weak blue CL that disappears during electron bombardment, whereas the bright blue CL of the Ti-

rich rim is stable; the numbers relate to the analytical points of spectral measurements; (**c/d**) the CL spectra of the Ti-poor hydrothermal quartz show a transient blue band at 440 nm (self-trapped exciton – STE) with strong decreasing intensity during electron irradiation and a slight increase of the 650 nm emission band (non-bridging oxygen hole center – NBOHC); the CL emission of the Ti-rich rim is dominated by a strong emission band at 440 nm that is stable under the electron beam and is possibly related to structural Ti.

Figure 13. CL spectra from Ti-poor quartz core versus Ti-rich rim in sample TiDi-24; the STE peak is clearly broader (FWHM 1.8 eV) compared to the Ti-rich rim (FWHM 0.87 eV) and enabling the FWHM of the ~450 nm emission to be used to differentiate the STE from the Ti^{4+} center; (note the Ti-poor core spectrum was smoothed using a 4-point running average).

Figure 14. Powder EPR spectrum of the original quartz (QTiDi-35) used for diffusion experiments showing the three centers $[AlO_4]^0$, E'_1 and $[TiO_4/H]^0$ and an unknown one, tentatively labeled as $[TiO_3]^-$ or Ti E'_1?.

Figure 15. Powder EPR spectrum of titanium diffused quartz (sample mix of QTiDi-23/24) after gamma-ray irradiation and measurement at 30 K and 30 dB; note that the spectrum shows only two centers ($[AlO_4]^0$ and $[TiO_4]^-$).

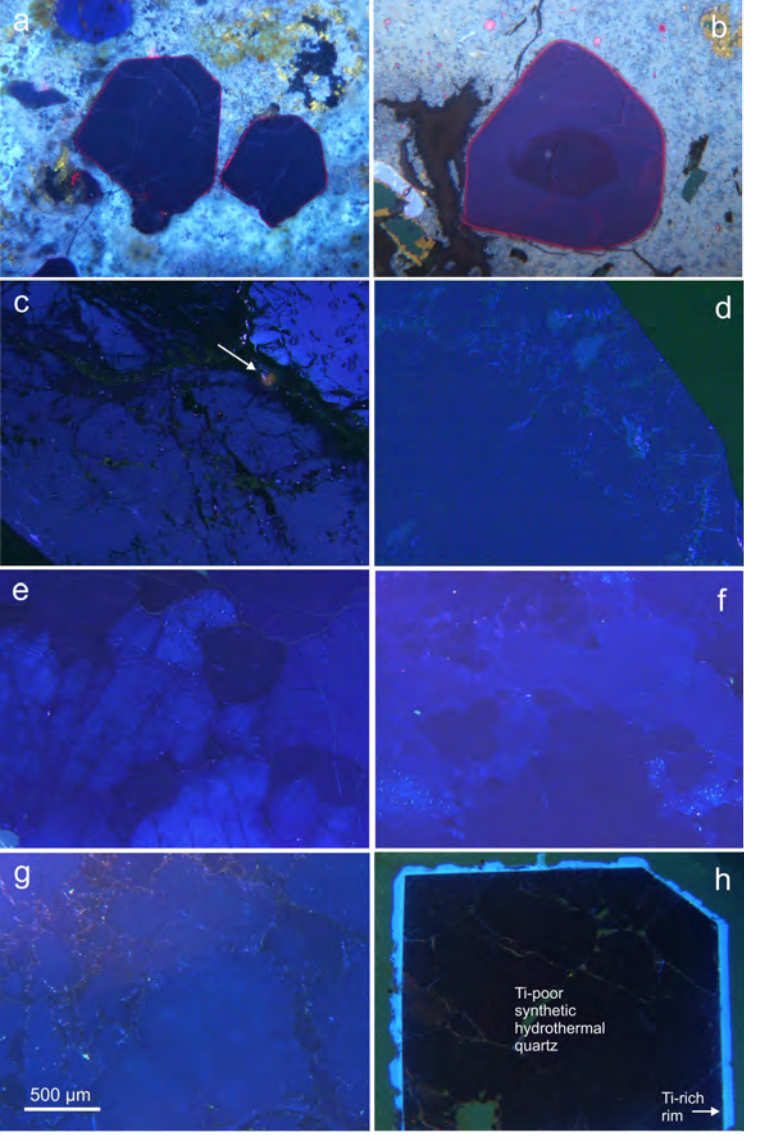
a
b
c
d
e
f
g
h
500 µm
Ti-poor
synthetic
hydrothermal
quartz
Ti-rich
rim

Figure 1

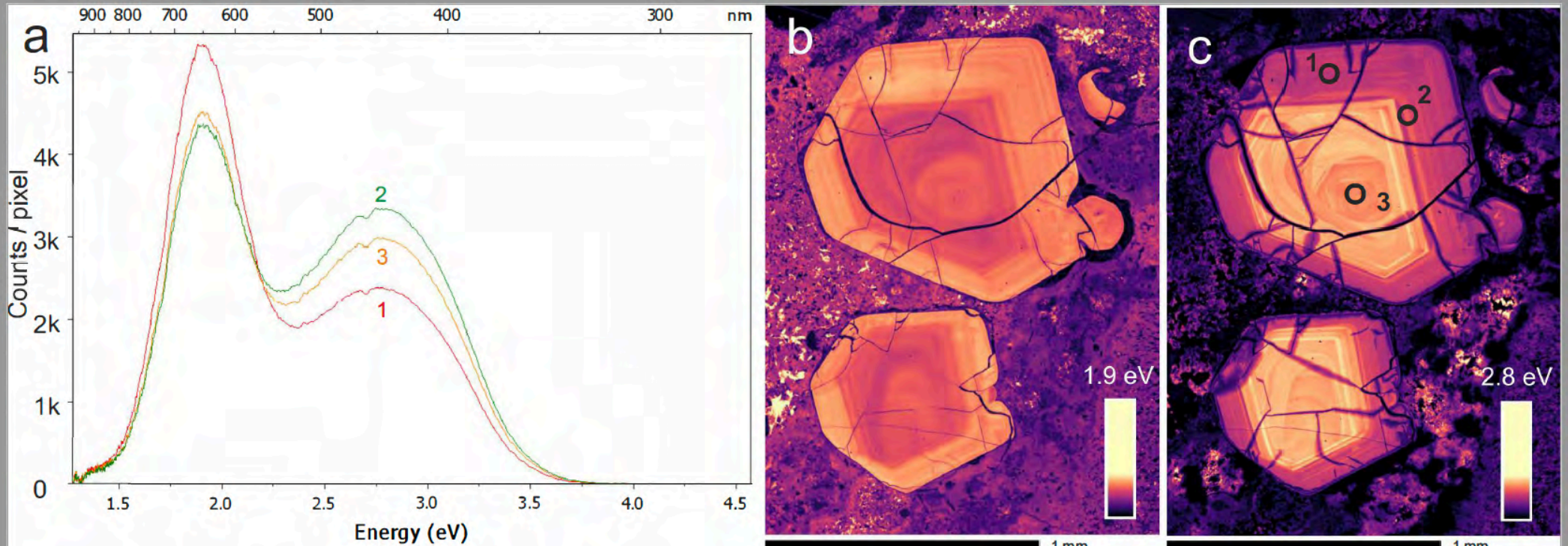
a
900 800 700 600 500 400 300 nm
5k
4k
3k
2k
1k
0
Counts / pixel
1.5 2.0 2.5 3.0 3.5 4.0 4.5
Energy (eV)
2
3
1
b
1.9 eV
1 mm
c
O 1
O 2
O 3
2.8 eV
1 mm

Figure 2

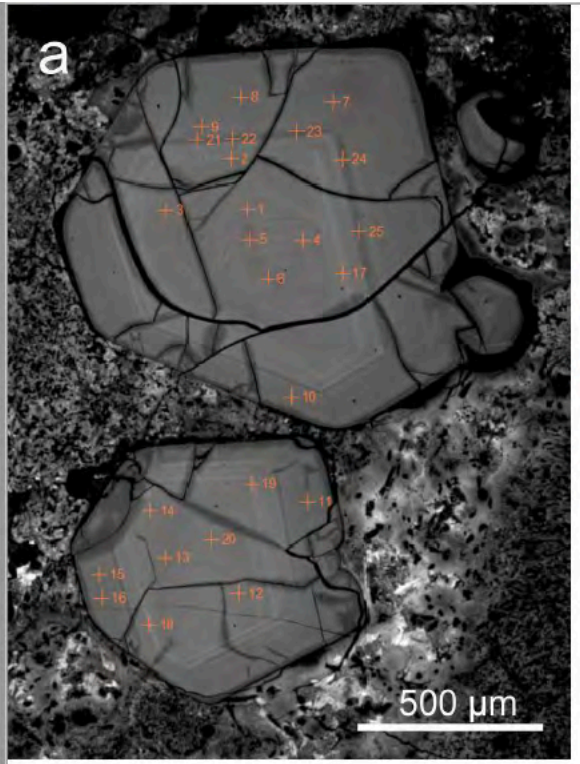
a
500 µm

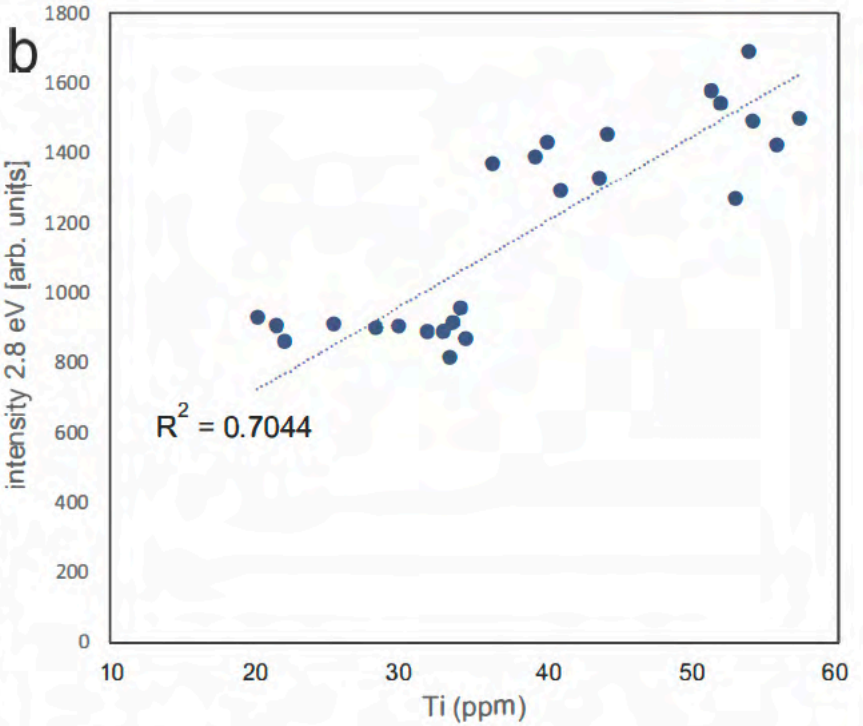
b
intensity 2.8 eV [arb. units]
Ti (ppm)
R^2 = 0.7044
0
200
400
600
800
1000
1200
1400
1600
1800
10
20
30
40
50
60

Figure 3

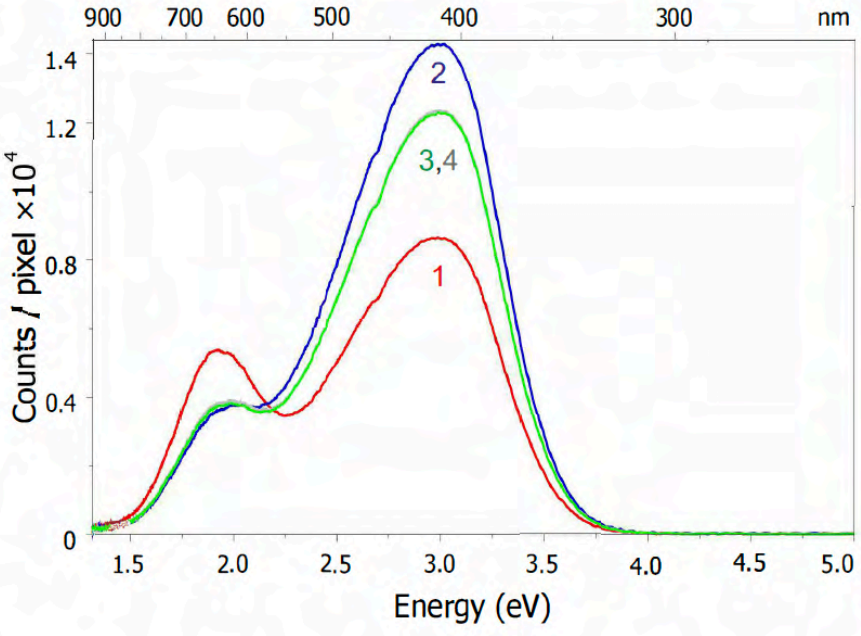
900
700
600
500
400
300
nm
1.4
1.2
0.8
0.4
0
Counts / pixel ×10^4
2
3,4
1
1.5
2.0
2.5
3.0
3.5
4.0
4.5
5.0
Energy (eV)

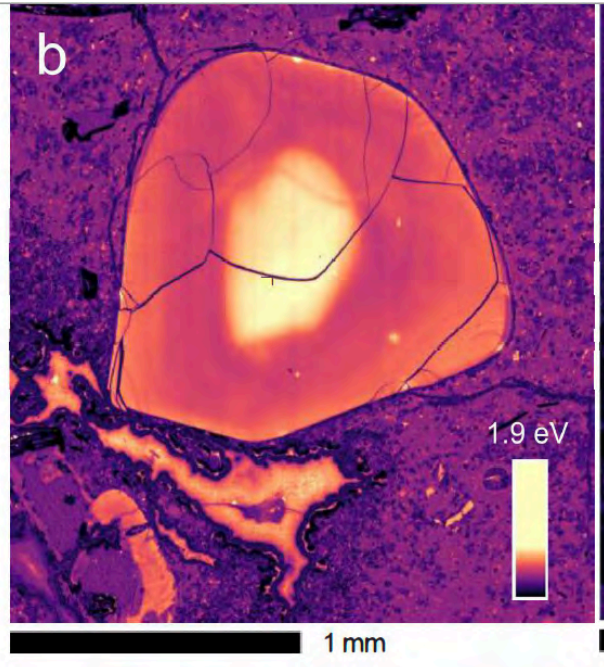
b
1.9 eV
1 mm

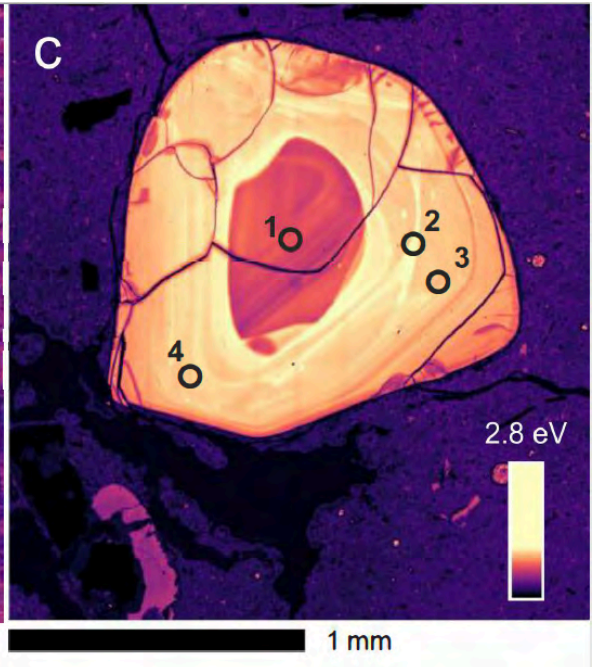
c
1
2
3
4
2.8 eV
1 mm

Figure 4

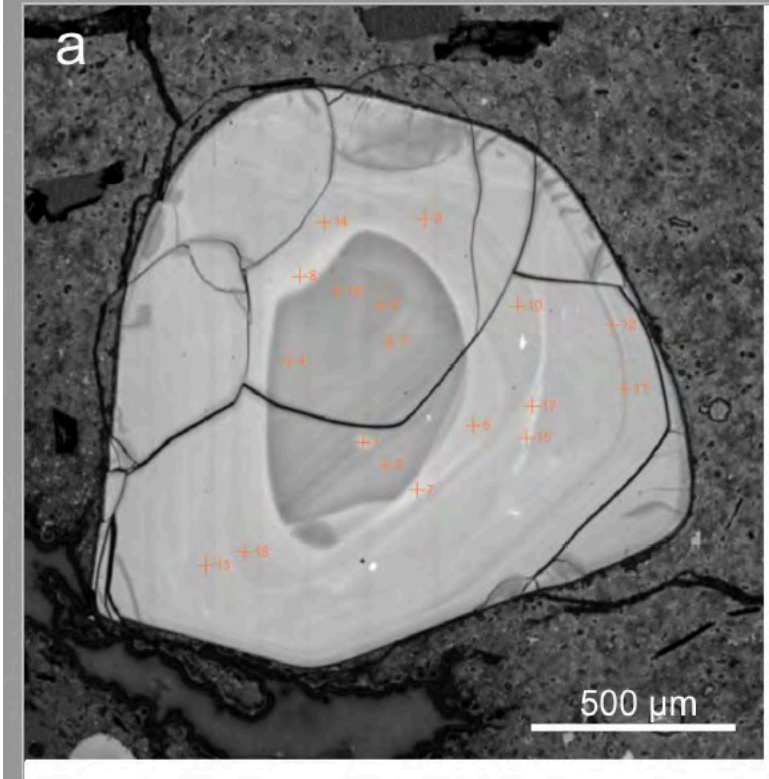
a
500 µm

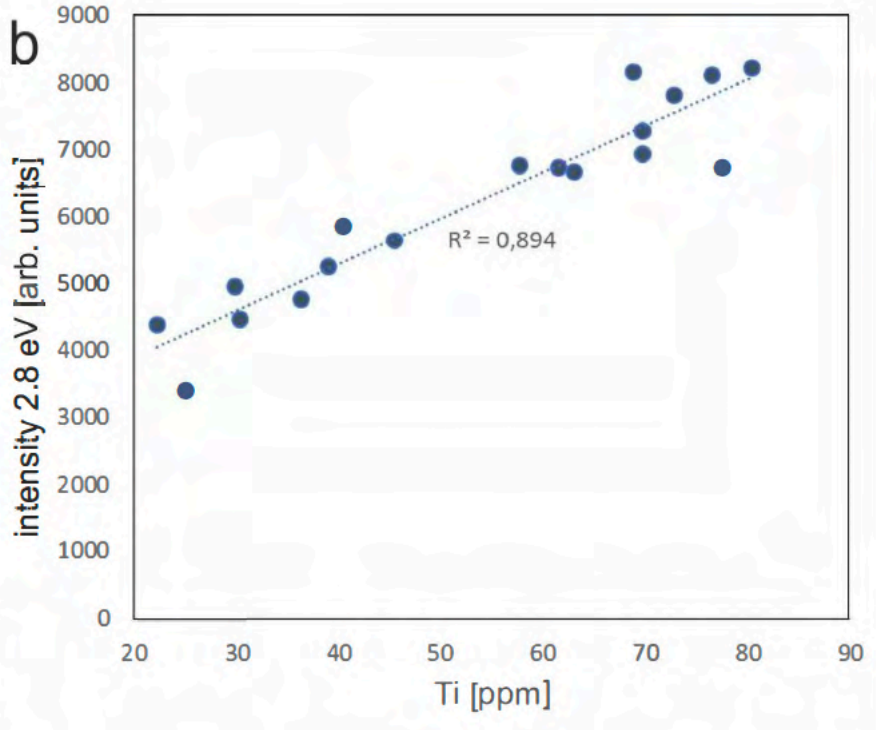
b
intensity 2.8 eV [arb. units]
9000
8000
7000
6000
5000
4000
3000
2000
1000
0
R² = 0,894
20
30
40
50
60
70
80
90
Ti [ppm]

Figure 5

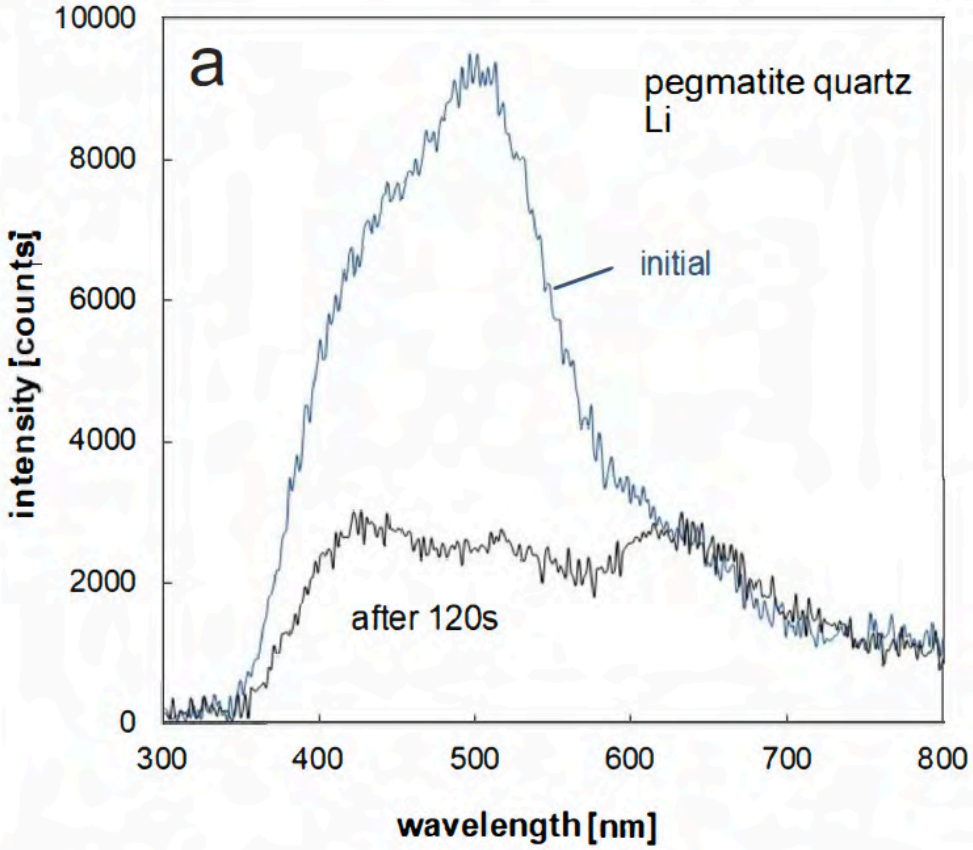
a
pegmatite quartz
Li
initial
after 120s
intensity [counts]
wavelength [nm]
10000
8000
6000
4000
2000
0
300
400
500
600
700
800

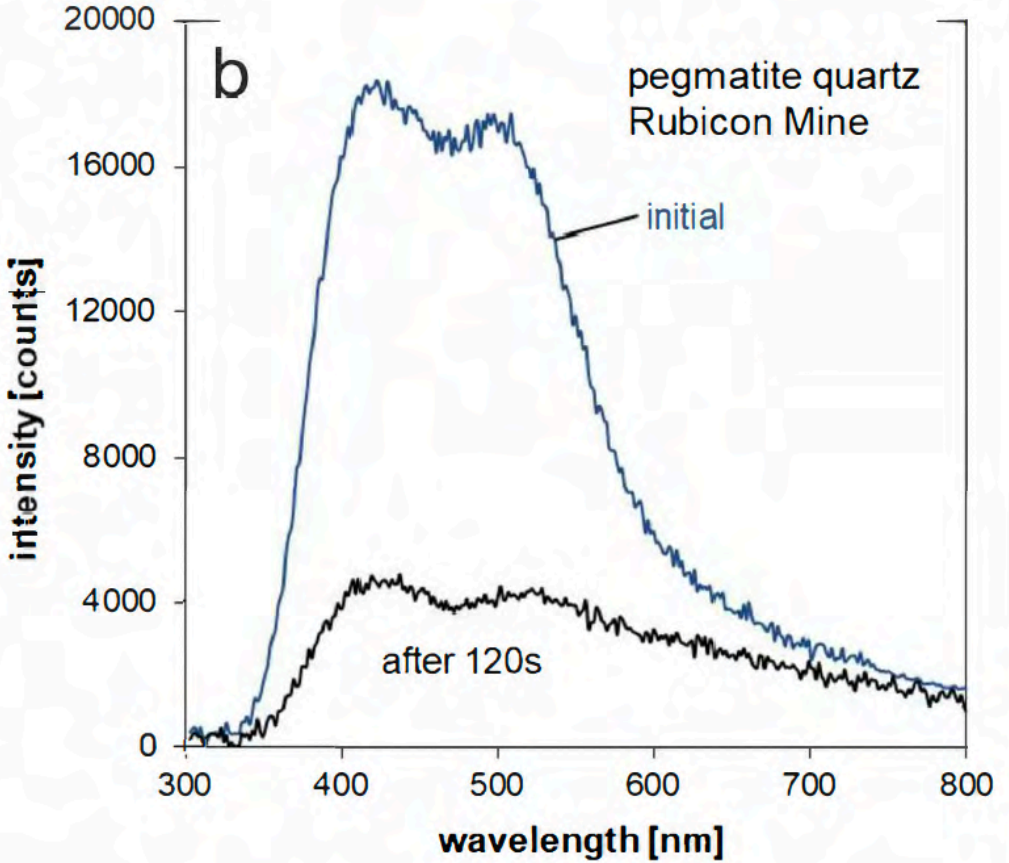
b
pegmatite quartz
Rubicon Mine
initial
after 120s
intensity [counts]
wavelength [nm]
20000
16000
12000
8000
4000
0
300
400
500
600
700
800

Figure 6

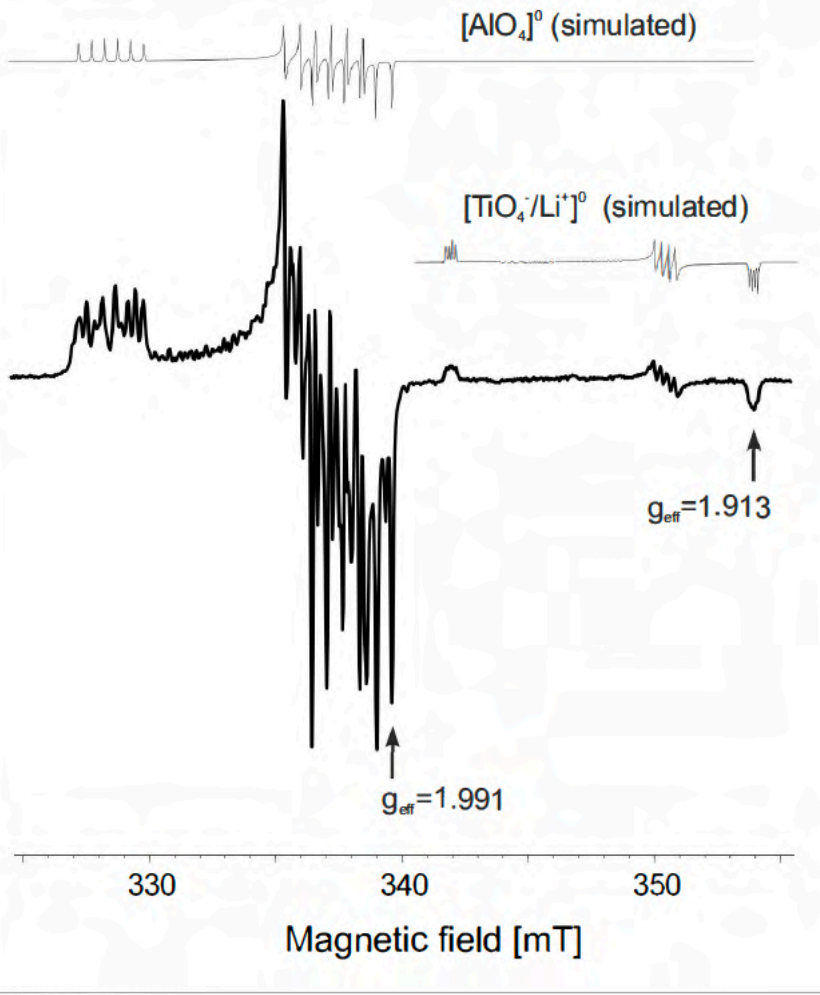
[AlO4]0 (simulated)
[TiO4-/Li+]0 (simulated)
geff=1.913
geff=1.991
330
340
350
Magnetic field [mT]

Figure 7

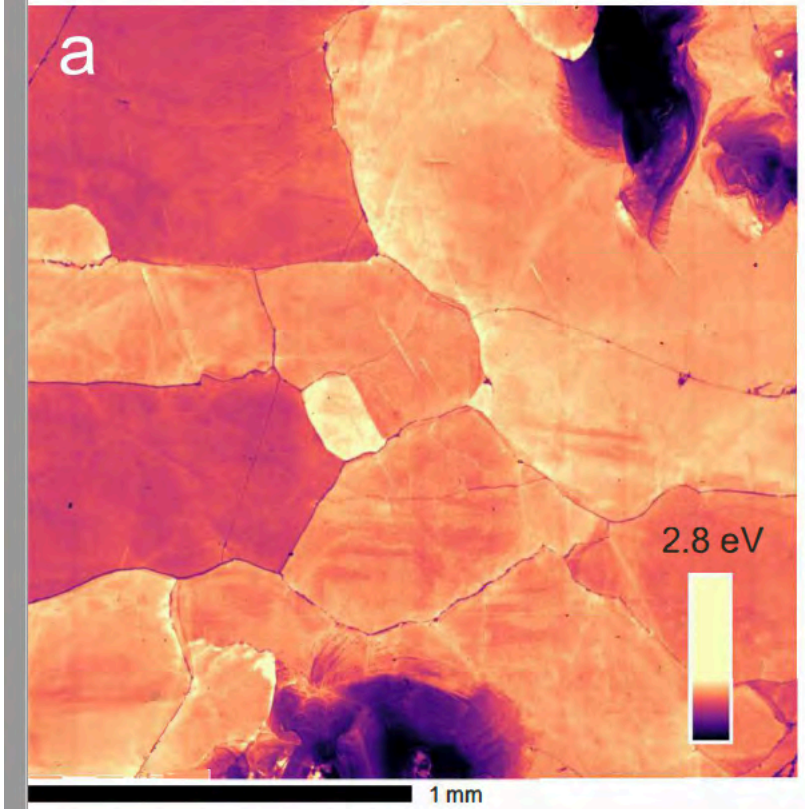
a
2.8 eV
1 mm

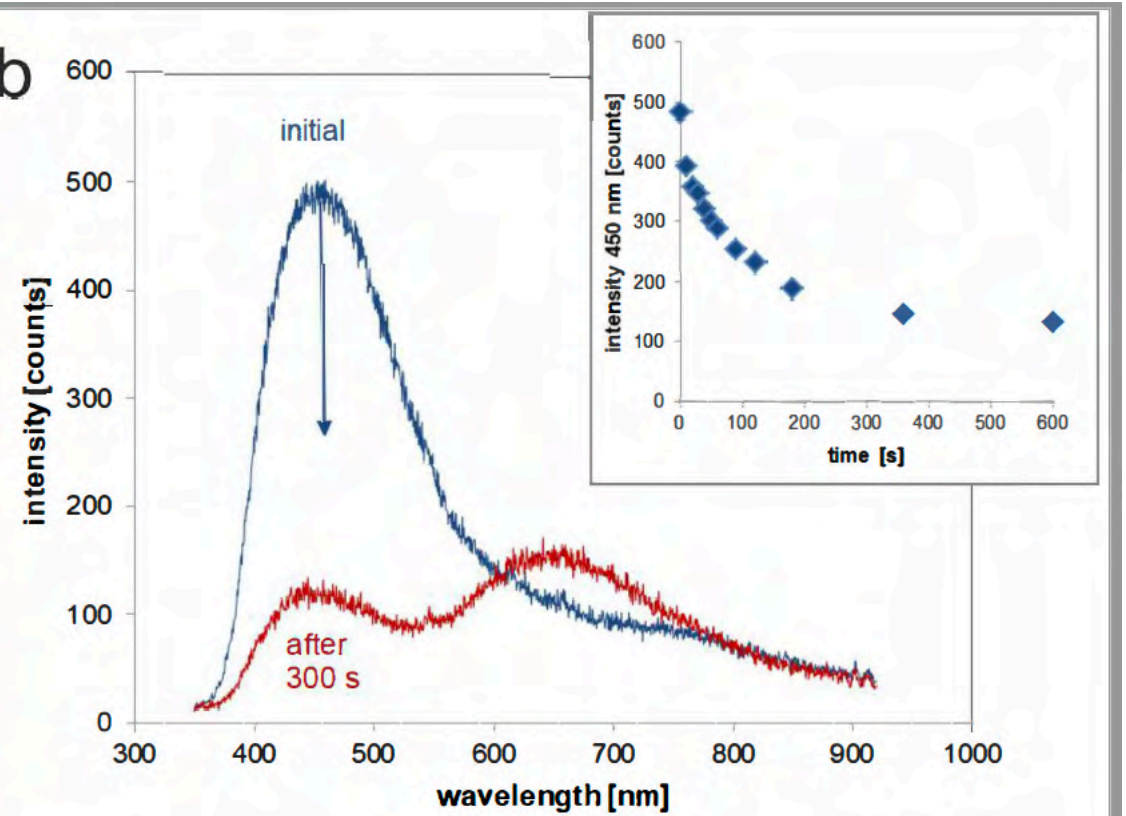
b
initial
after
300 s
intensity [counts]
wavelength [nm]
0
100
200
300
400
500
600
300
400
500
600
700
800
900
1000
intensity 450 nm [counts]
time [s]
0
100
200
300
400
500
600

Figure 8

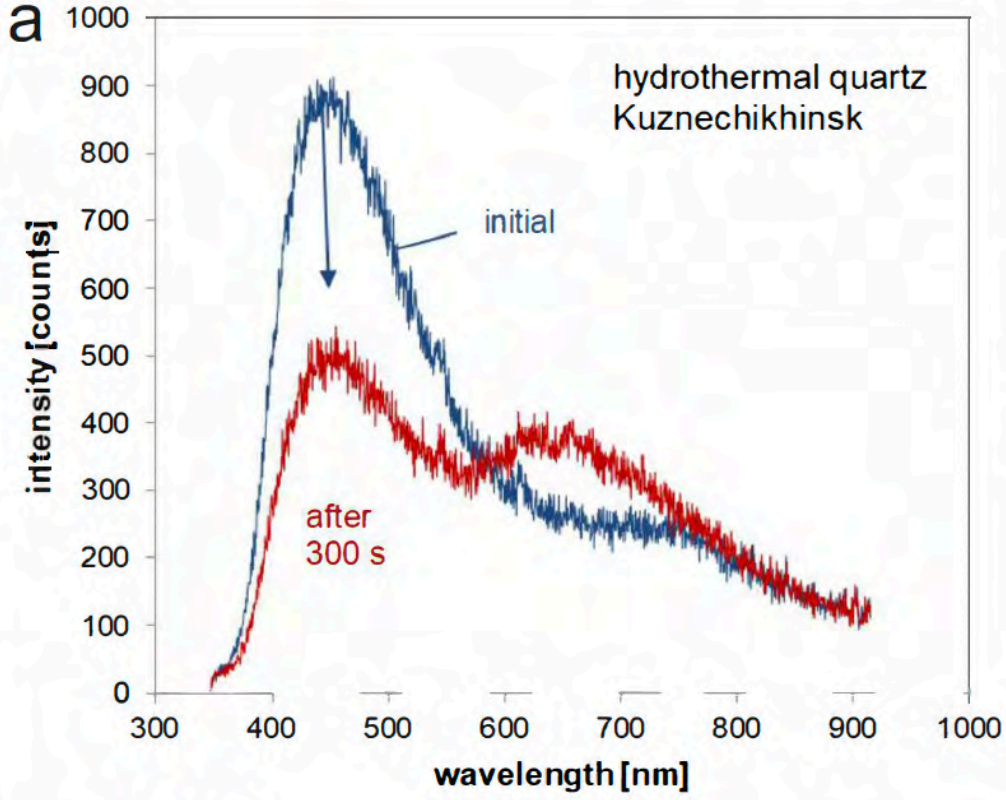
a
hydrothermal quartz
Kuznechikhinsk
initial
after
300 s
intensity [counts]
wavelength [nm]
0
100
200
300
400
500
600
700
800
900
1000
300
400
500
600
700
800
900
1000

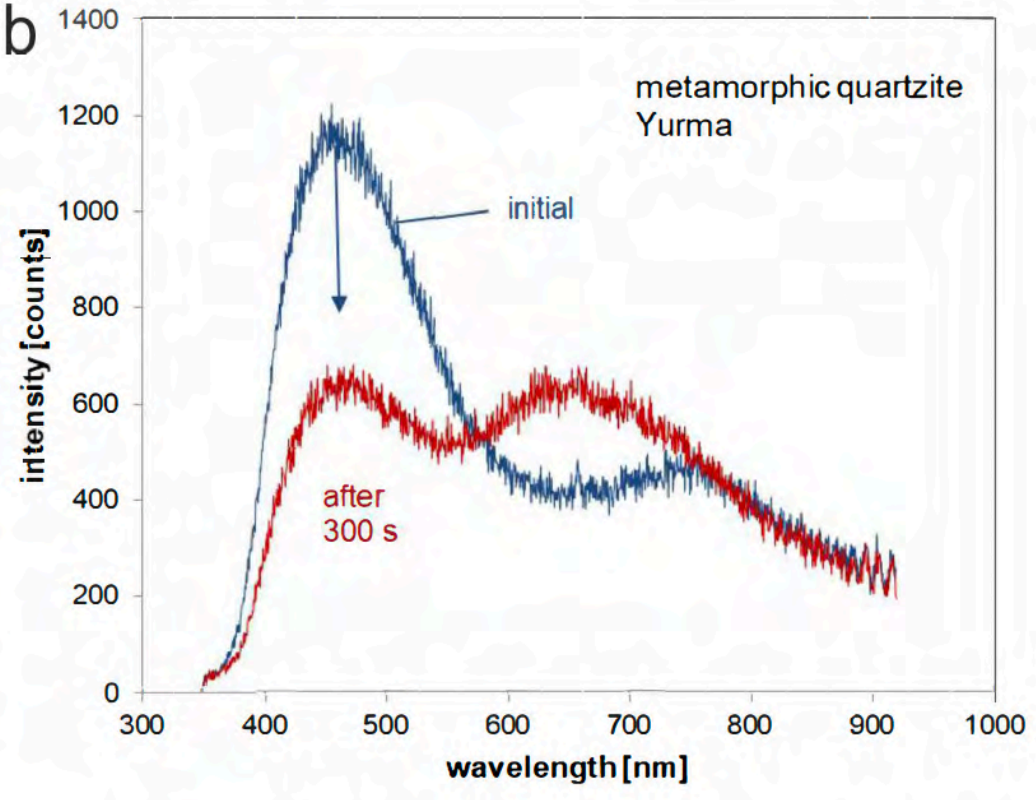
b
metamorphic quartzite
Yurma
initial
after
300 s
intensity [counts]
wavelength [nm]
0
200
400
600
800
1000
1200
1400
300
400
500
600
700
800
900
1000

Figure 9

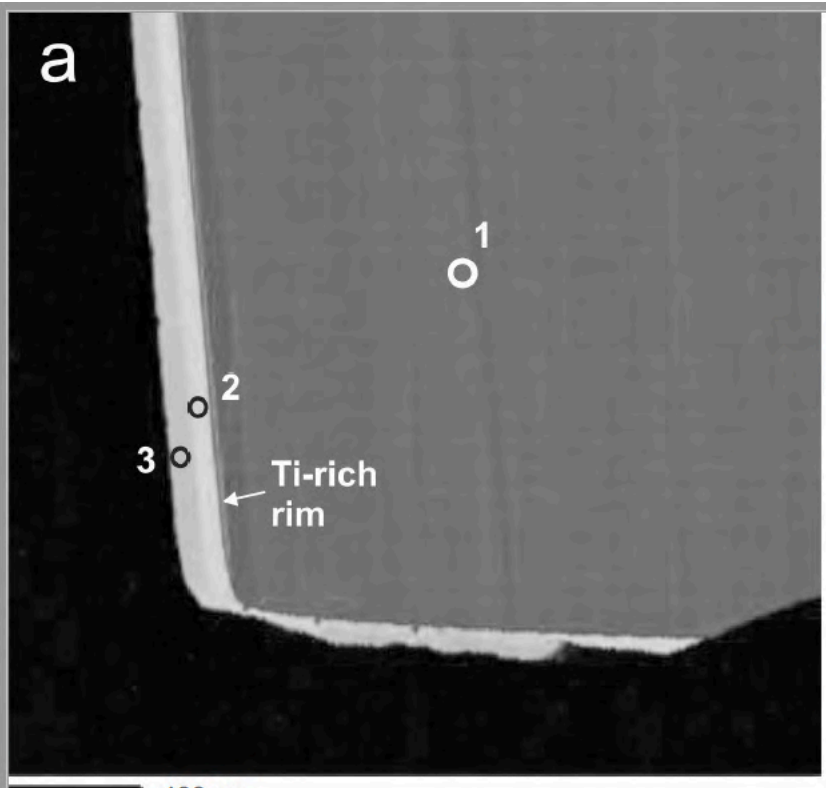
a
1
2
3
Ti-rich
rim
100 µm

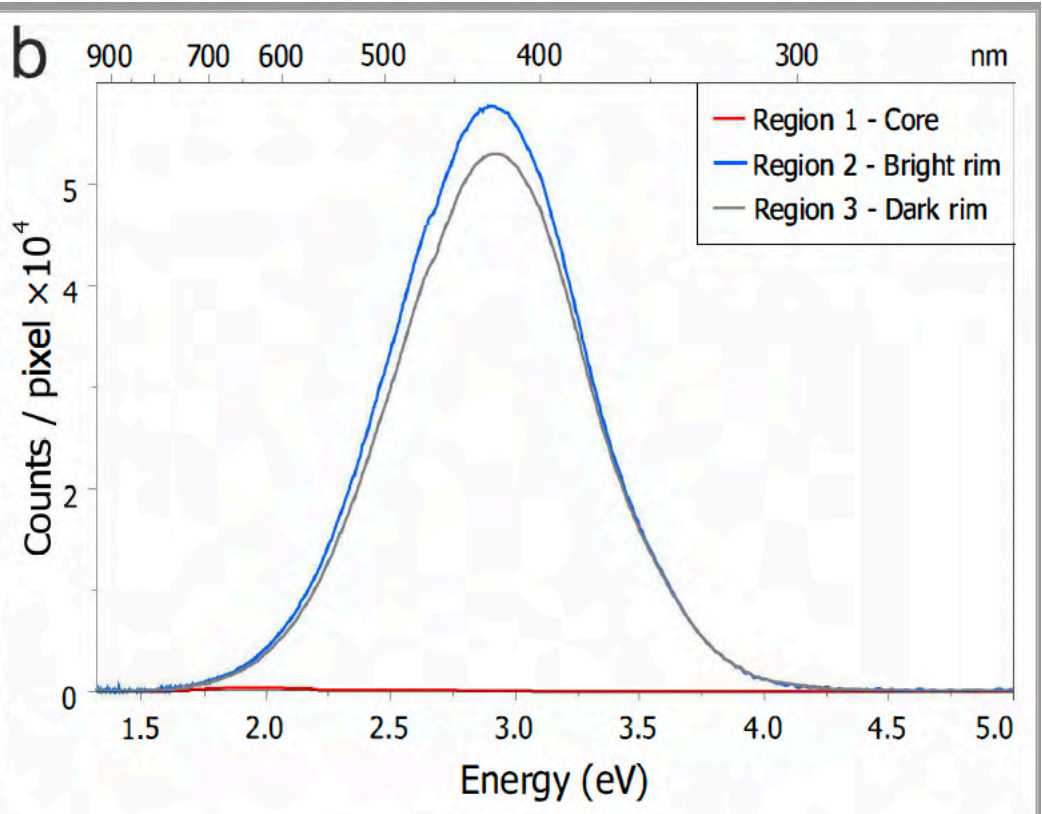
b
900
700
600
500
400
300
nm
Region 1 - Core
Region 2 - Bright rim
Region 3 - Dark rim
Counts / pixel ×10^4
0
2
4
5
1.5
2.0
2.5
3.0
3.5
4.0
4.5
5.0
Energy (eV)

Figure 10

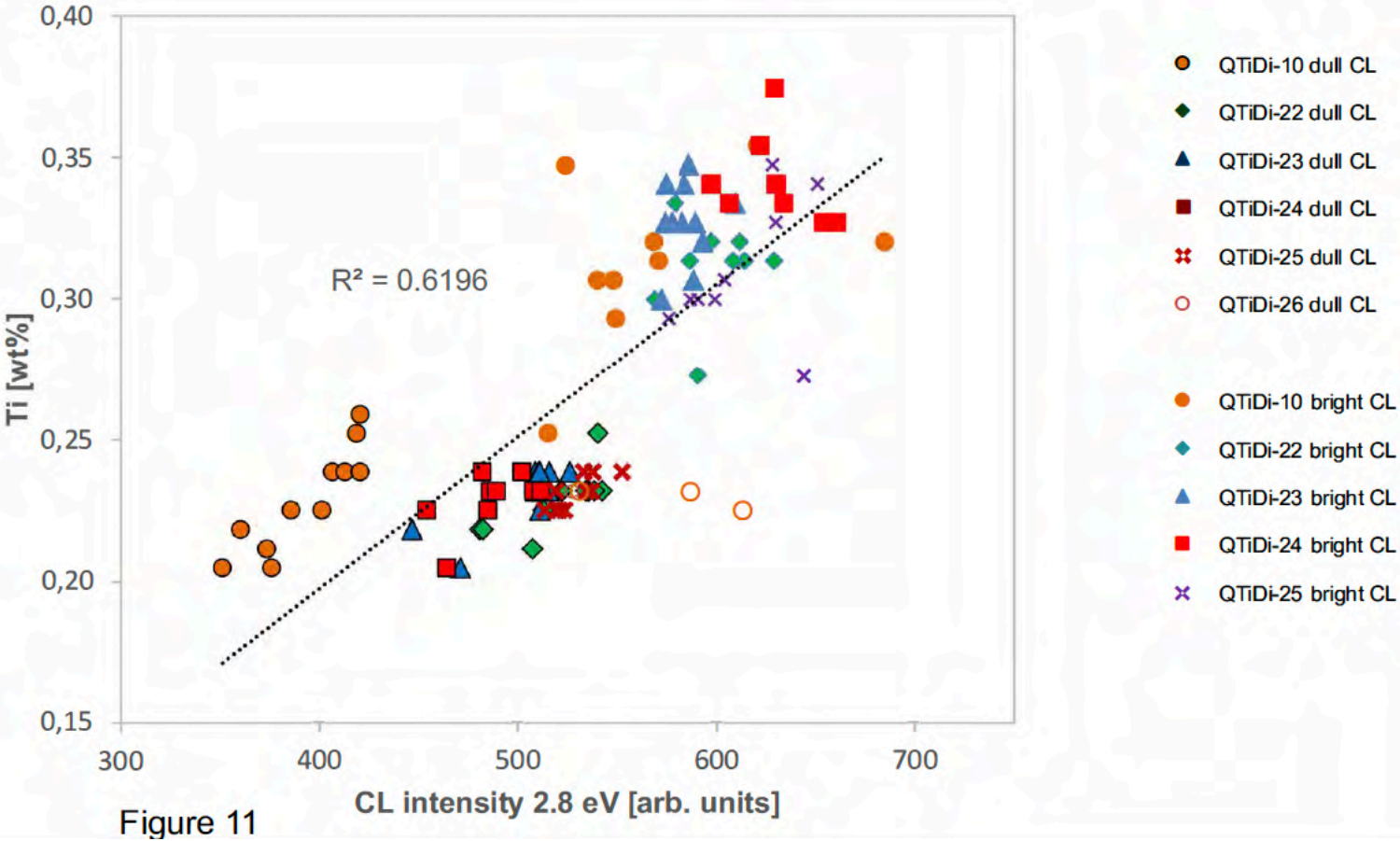
0,40
0,35
0,30
0,25
0,20
0,15
Ti [wt%]
R² = 0.6196
300
400
500
600
700
CL intensity 2.8 eV [arb. units]
QTiDi-10 dull CL
QTiDi-22 dull CL
QTiDi-23 dull CL
QTiDi-24 dull CL
QTiDi-25 dull CL
QTiDi-26 dull CL
QTiDi-10 bright CL
QTiDi-22 bright CL
QTiDi-23 bright CL
QTiDi-24 bright CL
QTiDi-25 bright CL

Figure 11

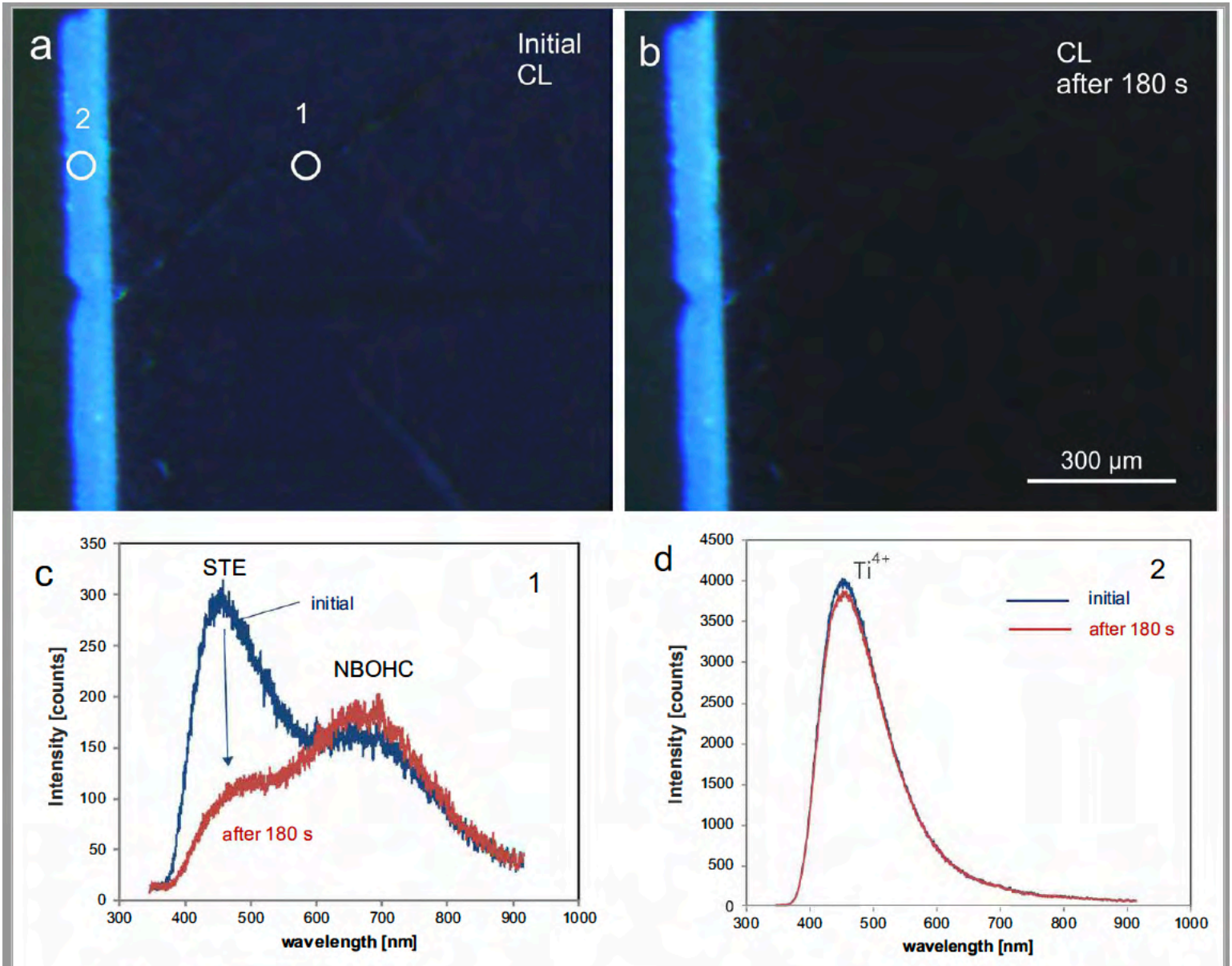
a
Initial
CL
2
1
b
CL
after 180 s
300 µm
c
STE
1
initial
NBOHC
after 180 s
Intensity [counts]
wavelength [nm]
d
Ti4+
2
initial
after 180 s
Intensity [counts]
wavelength [nm]

Figure 12

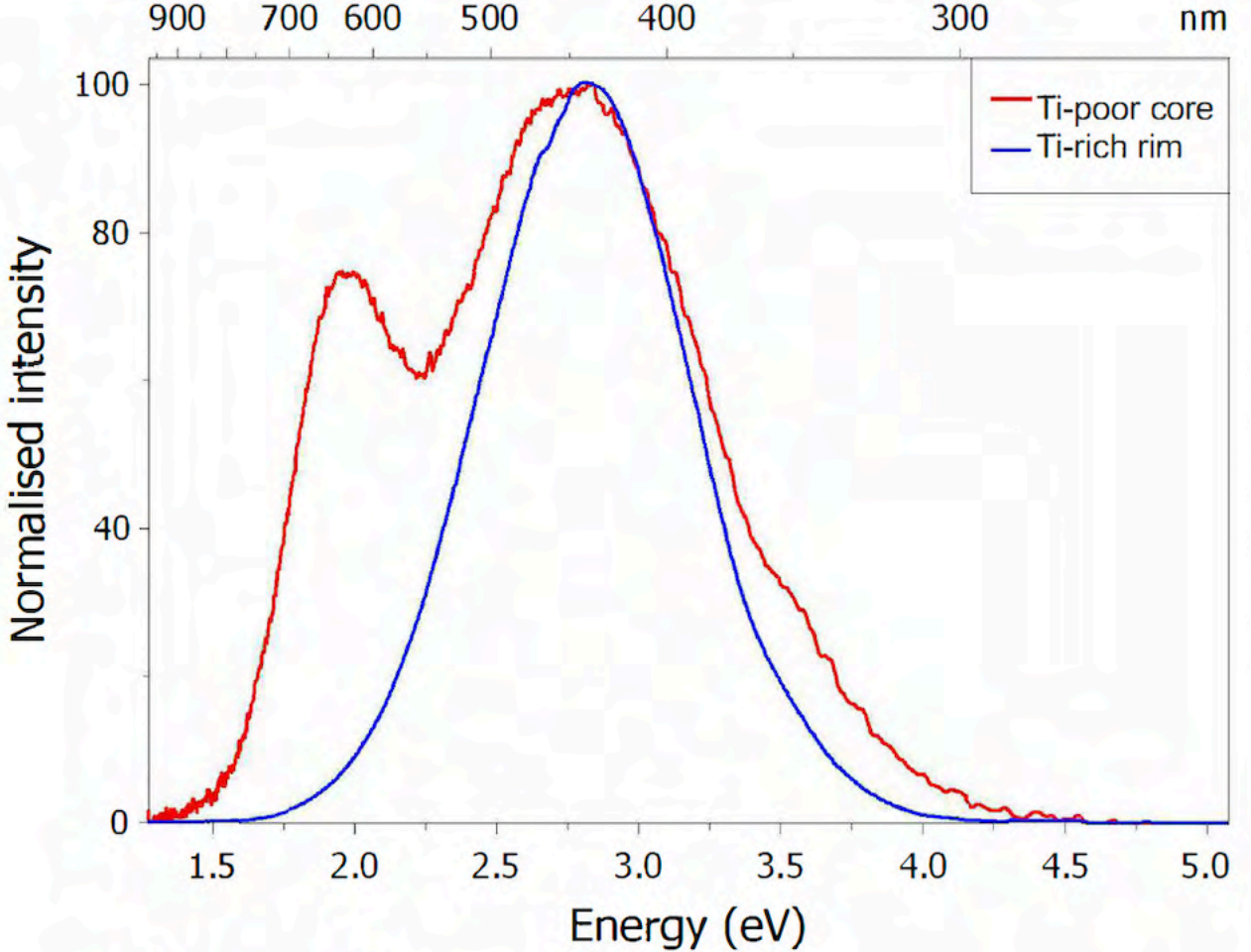
900
700
600
500
400
300
nm
100
80
40
0
Normalised intensity
Ti-poor core
Ti-rich rim
1.5
2.0
2.5
3.0
3.5
4.0
4.5
5.0
Energy (eV)

Figure 13

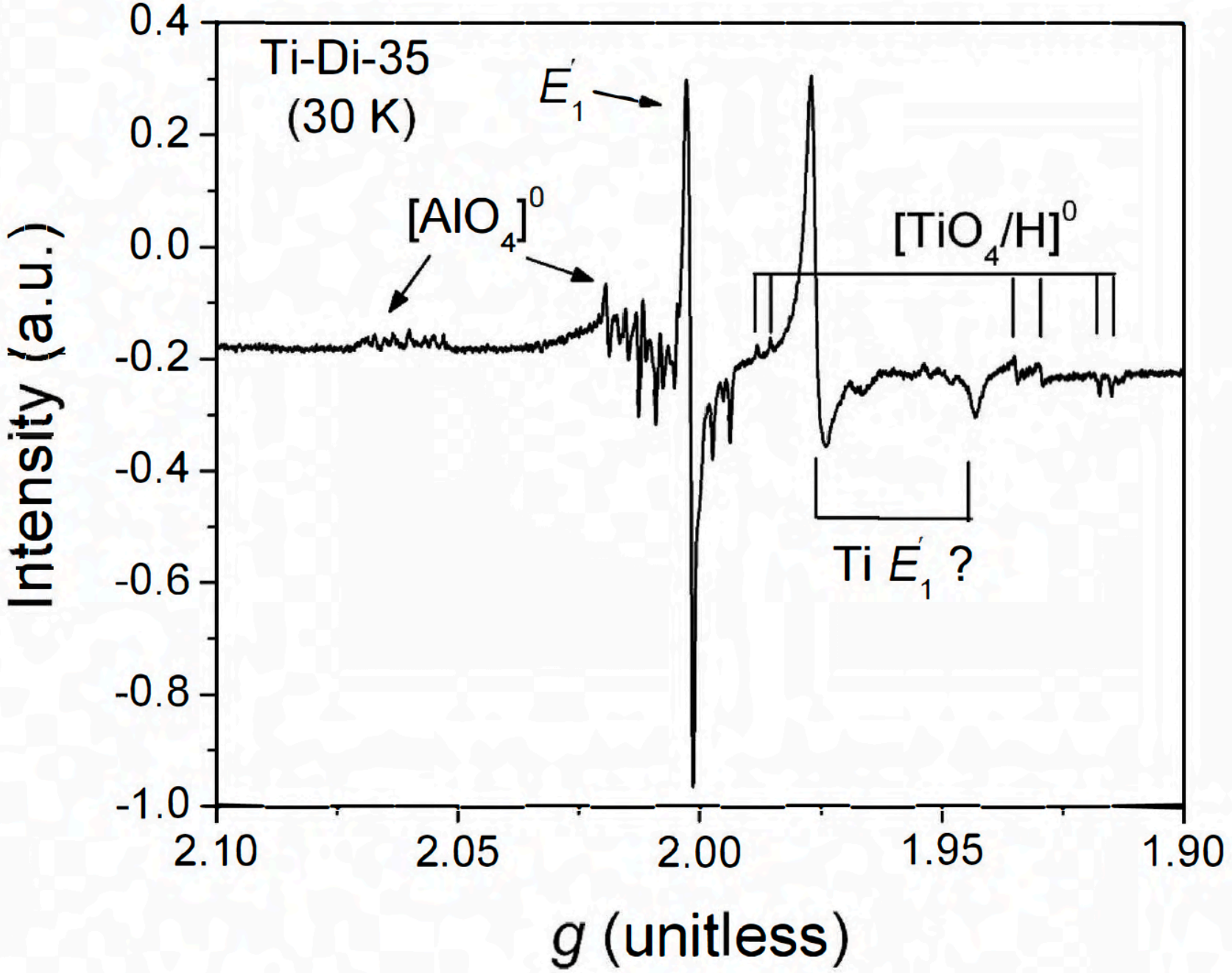
Ti-Di-35
(30 K)
E_1'
$[AlO_4]^0$
$[TiO_4/H]^0$
Ti E_1' ?
Intensity (a.u.)
0.4
0.2
0.0
-0.2
-0.4
-0.6
-0.8
-1.0
2.10
2.05
2.00
1.95
1.90
g (unitless)

Figure 14

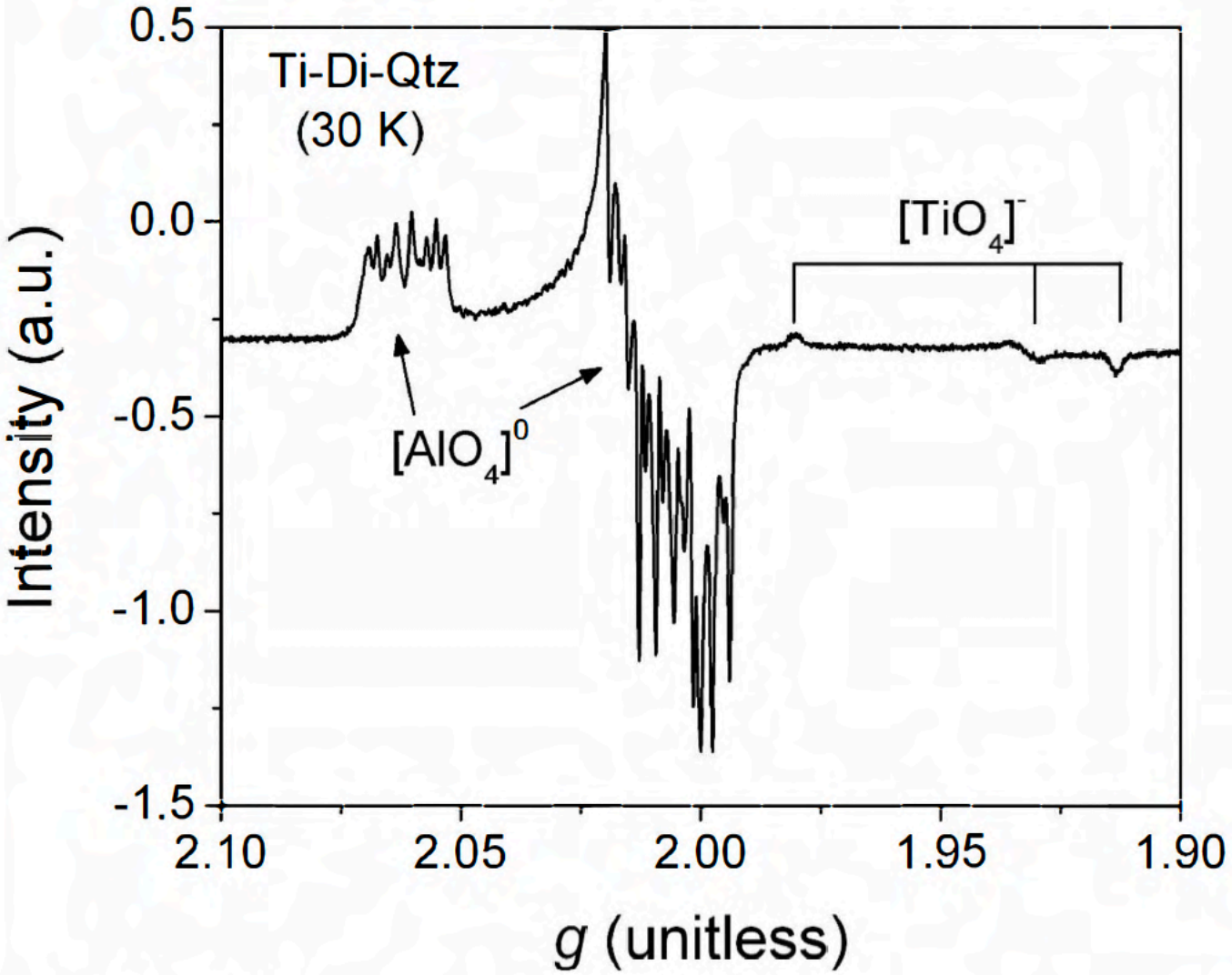
Ti-Di-Qtz
(30 K)
[TiO4]-
[AlO4]0
Intensity (a.u.)
g (unitless)
0.5
0.0
-0.5
-1.0
-1.5
2.10
2.05
2.00
1.95
1.90

Figure 15